Density effects resulting from polymer bonded explosives pressing parameters

MMK Alruwaily

Orcid.org/0000-0002-0919-8717

Dissertation accepted in partial fulfilment of the requirements for the degree *Master of Science in Mechanical Engineering* at the North-West University

Supervisor: Prof WL den Heijer

Graduation: May 2020

Student number: 27359840

ACKNOWLEDGMENTS

I would like to thank and acknowledge the following institutions and people who have provided me continuous support, not only during the research but also throughout the study of my master's degree.

Firstly, I would like to express my deepest gratitude to my supervisor Prof. Willem Den Heijer and my co-supervisor Dr. Rene Heise for their guidance, unwavering support and insight throughout this study.

Secondly, I thank Abdullatif Alshehri, Mesfer Al-Otaibi and Abdulelah Alhazani. Without their support and encouragements, this research project would not have been possible.

I would also like to thank Military Industries Corporation and Rheinmetall Denel Munition (Pty) for enabling this study by providing the funds and data. Also, the product development department for accommodating me, and their continuous support during my master's degree study.

Finally, special thanks go to my family and friends, without whose love and support, this study would not have been possible.

ABSTRACT

Shaped charges are used when a focused force is required to penetrate a target. They have dominated the weaponry market in the recent past due to their ability to penetrate targets. Shaped charges have become more potent and reliable as their technology has improved. However, the problem of uneven density distribution during the pressing stage of the manufacturing process remains. This is due to uneven particle sizes and ineffective pressing techniques, which affect the jet performance of the shaped charge. The aim of this study, therefore, was to predict the density distribution of a pressed polymer-bonded charge in an 85-mm casing. This was achieved via a numerical modelling technique that used a discrete element method (DEM).

This study employed DEM to model the pressing process of shaped charges. The experimental procedure involved the calibration of material input parameters (particle size, shape distribution, static friction coefficient, and bulk density). Calibration of the static coefficient was done using the angle of repose test. The experimental and numerical results were compared to determine the differences between the procedures and verify the calibration procedure. The numerical procedure used to model the experiments was DEM using AutoCAD and imported into Rocky® software. DEM, which was chosen because the consolidation process involved granular interactions, was used to simulate the pressing process system model.

The results showed that the density distribution in the casing had regions of low-density distribution, medium-density distribution, and high-density distribution. The regions close to the casing wall and the base of the bottom rammer exhibited medium density, while the regions closer to the wall (and in contact with the wall) had low density. Simulation results were verified and showed agreement with experimental result of Seloane (2018).

Based on the outcomes of this project, DEM was successfully used to predict the density distribution in shaped charges. Future studies should focus on investigating DEM using

different explosive materials and calibres. Consideration of future work should also include the incorporation of the particle distortion.

Keywords: shaped charge, density distribution, discrete element method, pressing process model

ABBREVIATIONS

AoR : Angle of repose

CT : Computed tomography

DEM : Discrete element method

FEM : Finite element method

LAMMPS : Classical molecular dynamics simulator

LIGGGHTS: Open source discrete element method particle simulation software

PBX: Polymer bonded explosive

RDM: Rheinmetall Denel Munition

2D: Two dimensional

3D: Three dimensional

LIST OF SYMBOLS

δ_{min}: The minimum overlap

δ : overlap

γ_0: Viscous damping coefficient

η_0: The damping coefficient

μ_n: Relative velocity following the normal direction

D : Distance between centres

e_i : The unit Vector

e : Void ratio

f^{hys} : Attractive forces

F_s : Shear force

F_n : Normal Force

F_x : The contact force components

f_i : Total forces

g : Gravtiy froce

I : The position of the particle

I_i : Momentum of inertia

k : The spring stiffness

k_s: Shear stiffness

k_n: Normal stiffness

k_1 & k_2 : Slopes of respective plots

M_x : Momentum

m_i : Mass

N : Consecutive times

n : Velocity normal

q_i : Torque/Couples

Rx : The radii of x disc

Ry : The radii of y disc

R : Coefficient of restitution

$\dot{s}$: Tangential component

t_i : The difference between two unit vector

t_t : The total Tourqe

t_c : Typical response time

v : Poisson's ratio

V_b : Bulk volume

Vs : Volume of solid

V_v : Volume of voids

ω_t : Angular velocity

$\tilde{x}$: Velocity vector of x particle

$\tilde{y}$: Velocity vector of y particle.

TABLE OF CONTENTS

LIST OF FIGURES

LIST OF TABLES

CHAPTER 1: INTRODUCTION

1.1 Background

A shaped charge is a cylinder-shaped explosive charge with a hollow cavity on one end and a detonator on the opposite end. Shaped charges were originally used in mining, where they were particularly suited to the task of making holes in rocky surfaces to access valuable minerals. Today, their applications have expanded to other areas, such as the demolition of buildings, the manufacture of steel products, and the creation of holes in hard surfaces. In addition to these areas, shaped charges are increasingly used in the military for warfare purposes.

A typical shaped charge has a detonator on one side and a highly reactive explosive on the other. When the detonator is activated, high-frequency waves are produced. These waves travel towards the apex of the liner, where they cause the liner to deform, releasing a high-speed jet along the axis of the cylinder (Lim, 2013). Once the jet makes contact with the target, it exerts pressure on it and produces heat (Goto et al., 2007).

1.1.1 Mechanism of shaped charge jets

The mechanism of a shaped charge is well-documented with abundant literature on the topic (Walters, 1989; Poole, 2005). Figure 1.1 illustrates the various components of a shaped charge that work in concert to produce the jet.

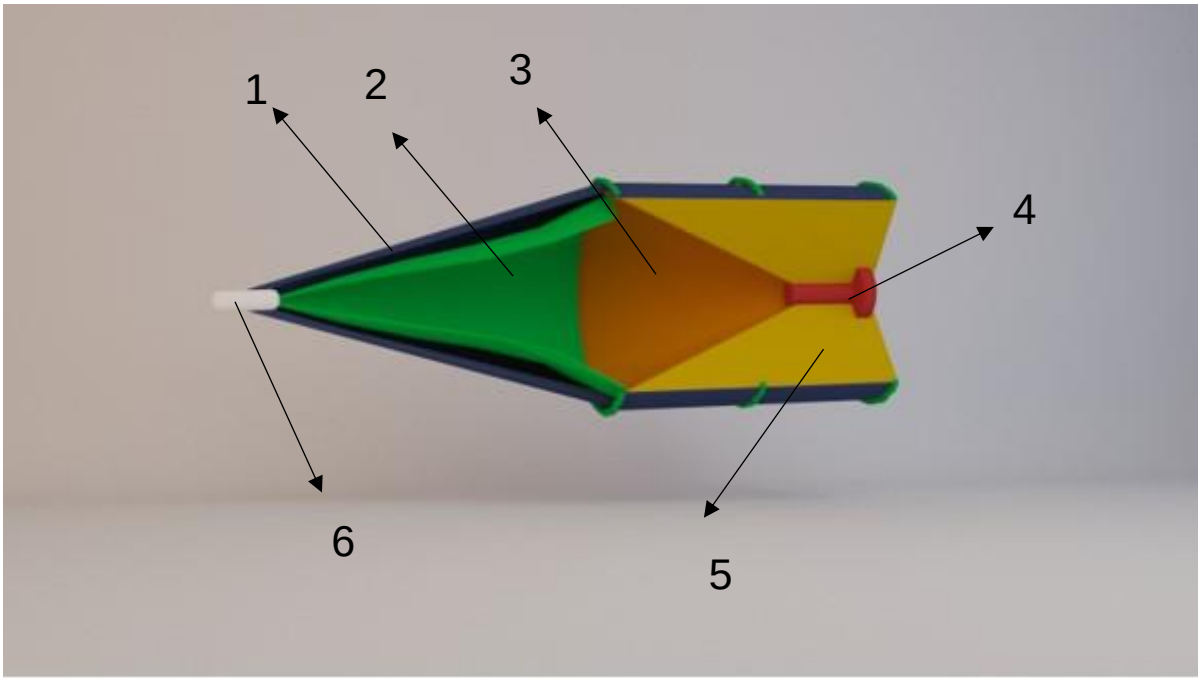

Figure 1.1: The structure of a shaped charge.

The following components can be observed from Figure 1.1:

1: Aerodynamic cover;

2: Air-filled space;

3: Conical liner;

4: Detonator;

5: Explosive; and

6: Piezoelectric trigger.

A shaped charge typically contains an explosive at one end of a tube-shaped structure and a detonator at the other end (Shi et al., 2016). The explosive material surrounds a liner, which, though often cone-shaped, may also take other shapes, including hemispherical, trumpet-, and tulip-shaped (Poole, 2005). The liner is commonly made of copper. However, other metals such as steel, zirconium, and uranium may also be used (Bourne et al., 2001; Held, 2001;

Saran et al., 2013). The composition of the liner depends on the application of the shaped charge.

The end of the liner closest to the detonator is called the apex (Poole, 2005). When the charge is ignited, a shock wave is generated. The wave moves toward the detonator, causing the expansion of the surrounding case, which results in fragmentation (Poole, Ockendon, & Curtis, 2002). The pressure of the detonation wave causes a process known as “collapsing” that results in extreme distortion of the liner (Poole, 2005). The liner’s collapse causes a jet to discharge from the shaped charge at a speed of between six to twelve kilometres per second (Poole, 2005; Ugrčić & Ugrčić, 2009). The tapering shape of the liner causes the jet to lengthen until it reaches the target. Generally, the longer the jet, the deeper the penetration (Poole, 2005).

The high pressure exerted on the target by the tip of the jet causes the target to deform via a plasticity effect (Poole, 2005). The exact temperature resulting from the contact between the jet and the target is not well known. However, some researchers argue that the average temperature on the surface of the target from contact with the jet is approximately 500 °C (Poole, 2005).

1.1.2 Applications of shaped charges

A shaped charge is used when a focused explosive force is required to pierce a target. Thus, shaped charges are extensively used in military applications for penetrating armoured targets and barriers (Elshenawy, 2012). Early shaped charges proved ineffective for this task due to the poor technology used to construct warheads at the time. For example, the precision of detonators was inferior, and the charges did not produce powerful jets (Kobylkin, 2015). As a result, early shaped charges could only penetrate light targets. However, research has led to numerous developments in shaped charge technology over the years, which has significantly improved their effectiveness. As a result, their usage has grown. The modern applications of shaped charges in the military include high explosive anti-tank (HEAT) munitions (Homel,

Guilkey, & Brannon 2015), as well as anti-tank guided missiles, unguided rockets, gun-fired projectiles, rifle grenades, land mines, and torpedoes (Poole, 2005).

Shaped charges are also used extensively in civilian applications. The oil industry, for instance, uses more shaped charges than the military annually (Poole, 2005). Here, shaped charges are used for perforating oil wells after the “cementing” process to obtain oil from neighbouring rocks (Poole, 2005). Other applications of shaped charges occur in industries such as mining (for tunnelling and rock drilling), demolition, explosive welding, avalanche control, and tree felling (Poole, 2005; Elshenawy, 2012).

1.1.3 Hydraulic pressing of shaped charges

The hydraulic pressing process used for manufacturing shaped charges relies on the Pascal principle, which argues that the stress exerted on one point of a blocked system is distributed equally in the entire object (Mahdian et al., 2013). Based on this principle, the pressure exerted by the high-frequency waves emanating from the explosive is disseminated uniformly throughout the entire surface of the liner. Consequently, each section of the liner is subjected to the same amount of pressure from the waves. The result is that the liner is deformed all at once across its entire surface, which causes the jet to fire in a straight line originating at the apex of the conical liner. The fact that the shape charge jet travels in a linear path reduces the charge’s chance of missing the target (a situation that can occur if the jet does not fire in the correct direction or is diverted before it reaches its target).

If Pascal’s principle did not apply, parts of the liner would deform at different times, and pressure would be applied unequally across the liner. This would result in a misaligned path for the jet, which could lead to missing the target. Even if the jet did not miss, however, a misaligned path could adversely affect the ability of the charge to penetrate its target. As noted earlier, the effectiveness of a shaped charge is determined by its ability to penetrate deep

inside the target. Therefore, any imprecision in the path of the jet can render a shaped charge ineffective.

1.2 Problem statement

Hydraulic pressing has been used for manufacturing shaped charges, as a proper method to fill the shaped charges with specified amount of explosives. The process of hydraulic pressing has potential problems in packing density distribution of the explosive material in shaped charges. Recently, conventional methods of hydraulic pressing face many problems of distributing the same packing density of an explosive material or compound on each side of the shaped charge. This is due to the mechanism of hydraulic pressing, which does not take into consideration the design of shaped charges. The design characteristics of the shaped charge is particular since it consists of curvatures. These curvatures obstruct equivalent explosive densities on each side.

1.3 Research objectives

This project models a consolidation process in order to predict the packing density using the discrete element method (DEM) to predict the density distribution of explosive materials or charges in a shaped charge. This will lead to improvement of the consolidation process to improve the shaped charge's performance.

The project has several specific objectives:

- To construct a model that represents the relationship between the pressing process and the density distribution of PBX material in an 81-mm shaped charge.
- To apply DEM simulations to predict the behaviour of explosive powders under consolidation, with the specific aim of identifying areas of significant packing density gradients during the pressing process.

1.4 Ethical considerations

The project was conducted within:

"*Permission has been obtained from all companies that participated in this research, prior to the collection and publication of data*."

1.5 Expected contributions of study

The expected contributions are as follows:

- The research will create new knowledge by developing a novel method for predicting the density distribution of small-calibre shaped charges before being pressed.
- The research will investigate the novel uses of DEM for modelling explosive consolidation.

1.6 Chapter summaries

Chapter 1 provides background information on shaped charges and presents the research problem. The aims and objectives of the study are also described. The ethical considerations are mentioned.

Chapter 2 discusses relevant research literature. Topics include the effects of density distribution on the performance of shaped charges, the prediction of density distribution via simulation, the processes used to uniformly distribute the density, and DEM.

Chapter 3 describes the formulation of the numerical model and governing equations within the DEM framework.

Chapter 4 explains the calibration method used. The experimental method and the data evaluation procedures are described. The results of the study and the verification of the study's methods are presented.

Chapter 5 introduces the DEM model of the pressing process for shaped charges. The selection of input data is briefly described. This is followed by the verification of the simulation results with the experimental result of Seloane (2018).

Chapter 6 provides an overview of the study. Final conclusions and recommendations are made, and the value of the research is described.

1.7 Summary

This chapter provides background information on shaped charges and the hydraulic pressing process used in their manufacture. In addition, it enumerates this study's research objectives and ethical considerations. The division of the various chapters of this dissertation is also provided.

The following chapter reviews relevant research literature to provide a theoretical foundation for this study and demonstrate this study's contribution to scholarly discourses.

CHAPTER 2: LITERATURE REVIEW

2.1 Introduction

In the ammunition industry, the pressing process is an established procedure used for manufacturing shaped charges. Charges of diameters up to 170 mm can be pressed at high rates, making this an efficient method for manufacturing (Saßmannshausen et al., 1989). However, high-performance shaped charges require ideal rotational symmetry and structural homogeneity. To achieve a denotation wave of the desired geometry, the density distribution inside a charge must be symmetric, and it must satisfy certain other structural specifications as well (Essig et al., 1991). Thus, theoretical and numerical simulations of the pressing process are invaluable for predicting the final density of the material (as well as any possible deformation) (Saßmannshausen et al., 1989). These simulations save time and resources required for the tiresome and expensive experimental testing that occurs during the initial phases of component design (Essig et al., 1991).

This chapter presents a systematic literature review of methods for modelling the pressing process. It describes the finite element method to predict density distribution, then discusses modelling by the discrete element method. The chapter then presents various methods for modelling compacted material.

2.2 Predicting density distribution by finite element method

To obtain charges of sufficiently high quality, the pressing process parameters must be adjusted to the properties of the compacted particulate solids (Tadmor & Gogoz, 1979; Saßmannshausen et al., 1989). During processing, material properties such as bulk modulus and density are functions of the pressure experienced by the material (Essig et al., 1991). To ensure maximum detonation velocity, a finished part should have a maximum density and a certain density gradient (Essig et al., 1991; Saßmannshausen et al., 1989). For these reasons,

numerical simulations and analytical predictions are used to generate vital information related to density and material deformation before the charge is pressed (Essig et al., 1991). Among the analytical methods that have been used to model the pressing process and predict density distribution in shaped charges is the finite element method (FEM).

Essig et al. (1991) simulated the pressing process of shaped charges using FEM. The authors built their simulation on these assumptions: (a) that the density anisotropies of pressed bodies of particulate material were directly related to the charge's pressure distribution during pressing; and (b) that the frictional forces between tool surface and granulates had a marked effect on the pressure distribution in the part. The governing finite element equations were derived using the principle of virtual displacements. This principle states that "for a body which is in static equilibrium, the virtual internal work created by the stresses and virtual strains equals the virtual external work done by the externally applied forces and their virtual displacements". Non-linear equations were used because the material tensor and frictional forces depended on the local stress; therefore, an iterative solution scheme was used.

The simulation was used to model two charges: a cylindrical charge (with an existing analytical solution) and a charge of complex geometry (Essig et al. 1991). The experiment also involved a (real) shaped charge with a diameter of 106 nm and involved compressing the explosive from the side opposite the conical aperture, as shown in Figure 2.1. The experimental results compared very well to those of the finite element simulation. This suggested that FEM was able to accurately predict the density inside the shaped charge. However, during the simulation of the pressing of certain complex charges, challenges related to the presence of singularities were observed. These include the formation of a stagnation point where cracks were sometimes observed.

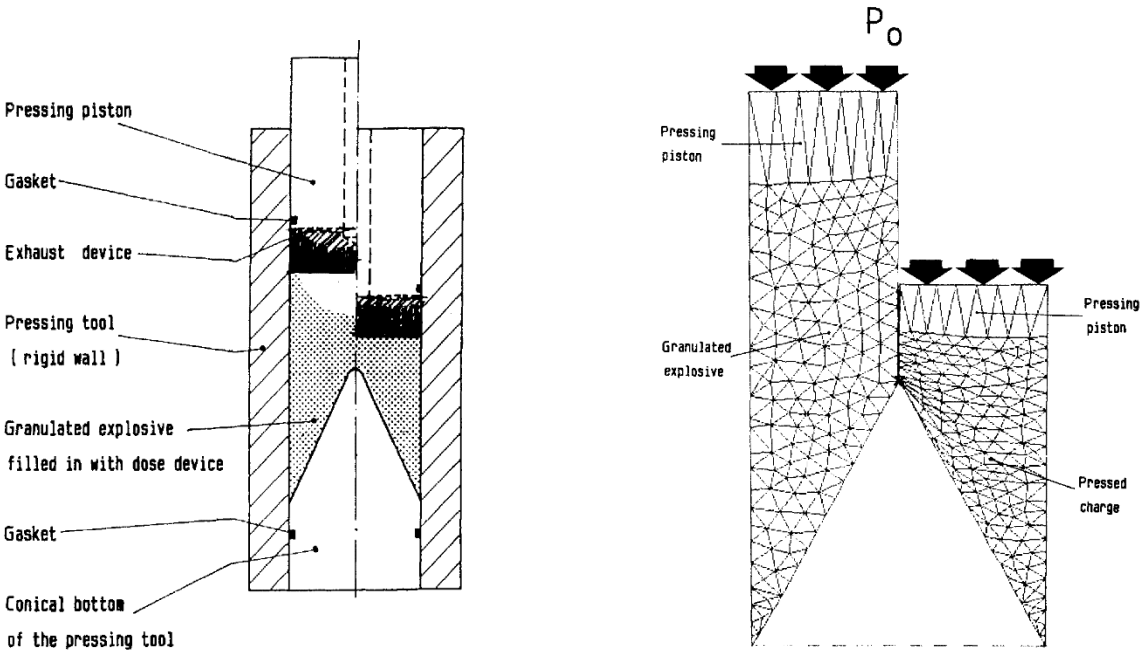

Figure 2.1: Illustration of the pressing process of a shaped charge (left), and finite element mesh of a charge before and after pressing (right) (Essig et al., 1991).

Other methods of modelling density distribution in shaped charges have also been applied. Saßmannshausen et al. (1989) proposed an analytical model that describes the density inside the charge as a function of the pressure and friction between the tool surface and the granule. The authors presented analytical calculations to accurately simulate the compaction of simple charges. Pressure distribution was modelled in a cylinder and a cone. Pressure distribution was approximated based the following assumptions: (a) the friction between the material and tool had been fully mobilized (i.e., the frictional forces were proportional to the normal forces); (b) the radial and axial stresses were considered the principal stresses; and (c) the cylinder radius was much smaller than the cylinder length (to ensure a constant radial stress) (Saßmannshausen et al., 1989). There was an exponential relationship between the pressure and the density of the compacted particulate solids, and the density was expressed as a function of pressure using the equation below.

$$\varrho = \varrho_F + (\varrho_0 - \varrho_F) \cdot e^{\beta \cdot P} \qquad (2.1)$$

Where ϱ_0 is the density of the uncompacted particulate solid, ϱ_F is the highest possible density, β is a compressibility coefficient, and P is the pressure.

For more complex geometries, finite element calculations are necessary and 2D or 3D tensors should be used. In Saßmannshausen et al. (1989), numerous cylindrical charges were pressed with different diameters and various pressures, and the bulk density and grain distribution of the explosive (wax coated RDX) were analysed. There was a strong correlation between the model and the experimental results for smaller diameters. The authors presented analytical calculations to accurately simulate the compaction of simple charges. For more complex states of stress, the authors developed a finite element program which takes into consideration frictional forces between the tool surface and material.

2.3 Computed tomography scan

A computed tomography scan uses computer-generated combinations of X-ray images taken from different angles to produce cross-sectional (tomographic) images of that resemble virtual "slices" of a scanned object. This process allows the user to see inside the object without cutting (Yang, 2009). Sinka et al. (2003) used an x-ray CT to measure the material density distribution in pharmaceutical tablets. For a given material and x-ray energy level, x-ray attenuation is approximately proportional to material density.

Seloane (2018) performed a study to investigate the density variations within explosive specimens in 81 mm shaped charge. Seloane measured the density of the pressed PBX material in 81 mm shaped charges, then conducted x-ray experiments using an explosive material substitute (a dummy material with similar material properties to PBX). Figure 2.2 shows the experimental result of a CT scan done by Seloane (2018). The scan finds a high-density area in the centre section between the top rammer and bottom rammer and low-density areas near the casing. Medium-density areas are found in the top corners and bottom corners. Note that this project uses Figure 2.2 to verify results of its simulation models.

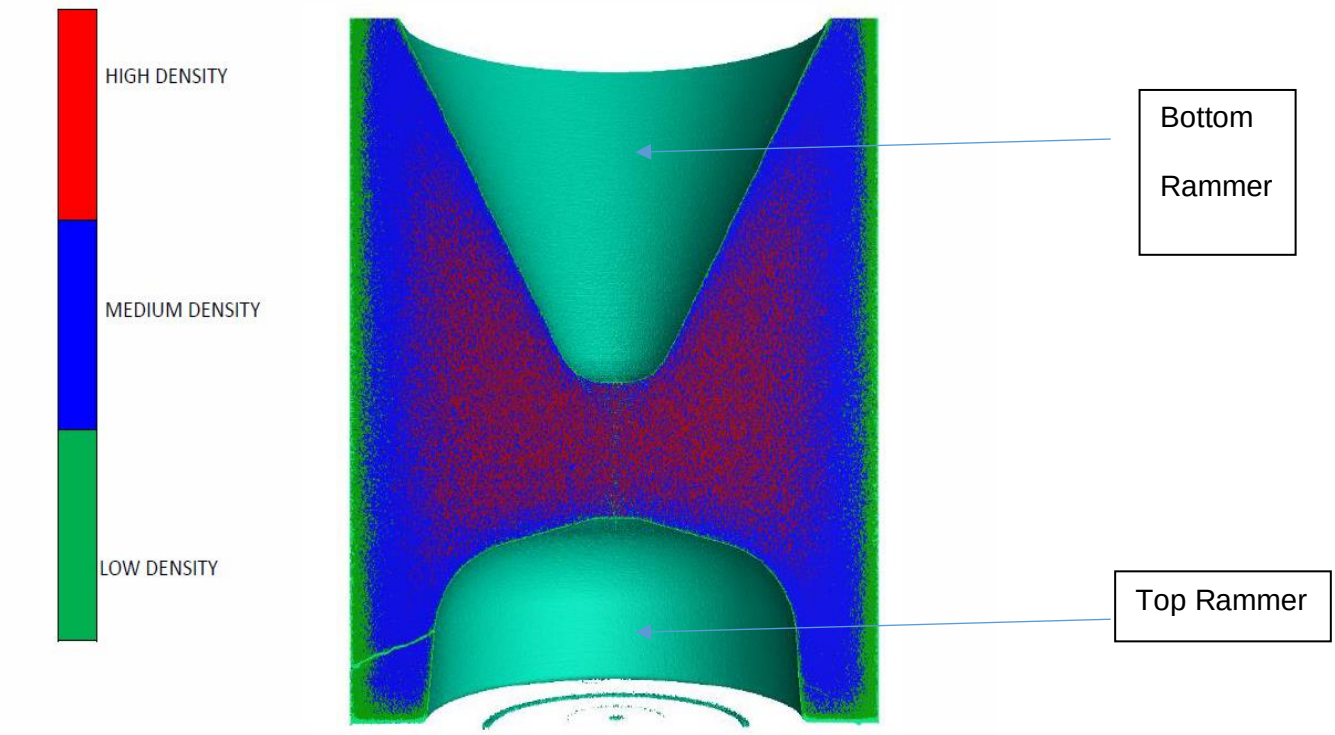

Figure 2.2: Computed tomography result for density distribution in a pressed 81-mm casing (Seloane, 2018).

2.4 Modelling by discrete element method

The discrete element method has become the preferred method for engineers and modellers validating and optimizing bulk material system designs (Gröger & Katterfeld, 2006; Coetzee, 2016). The main affordance of DEM is that the motion of granular materials is modelled as the motion of discrete particles (Cundall & Strack, 1979). Thus, DEM enables the investigation of granular material's mechanical behaviour at both macro and micro levels (Yan, Yu, & McDowell, 2009). Macro properties of material refer to bulk properties that are measurable, such as bulk density, penetration resistance, angle of repose (AoR), and bulk stiffness, among others (Coetzee, 2016). Micro parameters, conversely, are those parameters that are used by a specific DEM to model the material. These include, for example, particle density, particle

stiffness, and particle-particle friction coefficient (Coetzee, 2016). Often, micro parameters are not measured, and their values are simply assumed (Asaf, Rubinstein, & Shmulevich, 2007). Before DEM modelling can be confidently attempted, a set of accurate values of material input parameters is required. Thus, robust calibration techniques that are both experimentally and numerically efficient are necessary (Coetzee, 2016).

2.4.1 Calibration of material parameters in discrete element methods

DEM calibration principally involves changing the undefined parameters until an acceptable match is obtained between the results of the simulation and the physical measurements of interest (Rackl & Hanley, 2017). Often, calibration is performed using the relatively inefficient method of trial and error. Due to the significant weaknesses of calibrating DEM input parameters using trial and error, alternative methods have been developed (Rackl & Hanley, 2017). Numerous calibration procedures for DEM have been reported.

Rackl and Hanley (2016) described a new calibration method that is employs Kriging and Latin hypercube sampling. The authors demonstrated the effectiveness of a new calibration technique for DEM model parameters based on bulk density and AoR tests. The bulk material used were spherical glass beads. The simulations were conducted using the LIGGGHTS DEM code (public version), and the Hertz-Mindlin contact model (Rackl & Hanley, 2016). For each simulation, a critical time-step was incorporated and calculated using Equation 2.3 below.

$$dt_r = \frac{\prod r \sqrt{(p/G)}}{0.1631v + 0.8766} \quad (2.2)$$

Where p is particle density, G is shear modulus, r is the radius of the smallest particle, and v is Poisson's ratio.

The responses calibrated included the Rayleigh time-step, AoR, and bulk density. To obtain these responses, simulations were performed using the system shown in Figure 2.3 below.

Every simulation was conducted in the following way. 5 mm diameter particles were poured into the cylinder to a height above 50 mm under gravity, and the system was allowed to settle. Particles that came to rest above the 50 mm line were removed from the simulation field and the system was allowed to settle again. The cylinder was then elevated at constant speed in order to form a heap under gravity. Monochrome screenshots of the top-down viewpoint and side view were produced after the system had settled (Figure 2.4). The AoR and bulk density of the heap were determined using a verified image processing algorithm and were compared to values in literature for glass beads (Rackl & Hanley, 2016).

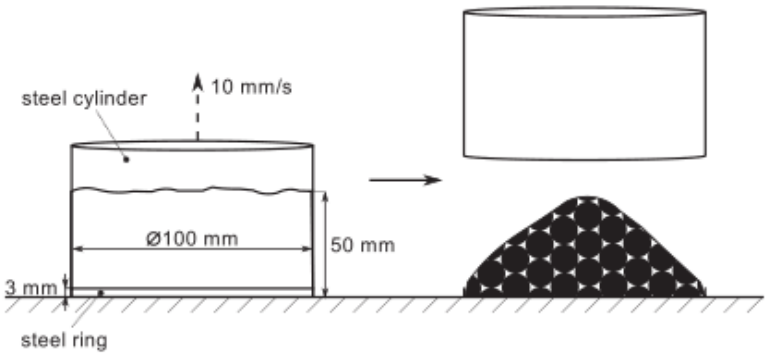

Figure 2.3: Schematic of the 3-D simulated system used to measure bulk density and AoR (Rackl & Hanley, 2017).

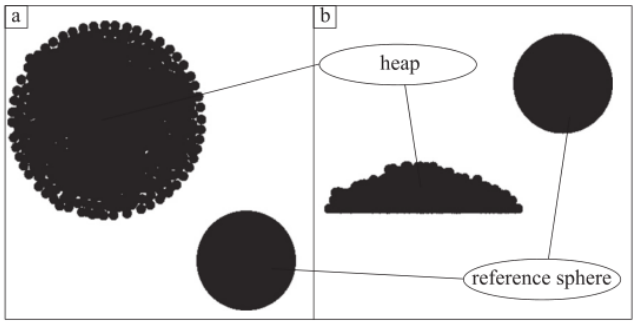

Figure 2.4: Top-down view (a) and side view (b) of an exemplary heap (Rackl & Hanley, 2017).

The calibration process involved Latin hypercube sampling, an adapted universal Kriging meta-modelling technique, and numerical optimization. The three phases of the calibration

process used are shown in Figure 2.5. In the initial sampling phase, a set of sample parameters are generated based on Latin hypercube sampling and forwarded to DEM models, then response data are collected. In the 1st optimization phase, parameterization of the Kriging meta-models is performed for the sample parameters and their responses. The optimization process is then initiated using these meta-models. Lastly, in the 2nd optimization phase, optimal parameters are used as starting values for optimization in the actual DEM models.

The authors' calibration procedure was reliable and resulted in satisfactory calibration outcomes. The calibration for bulk density was particularly accurate. The AoR was more scattered. However, most runs had values within the maximum tolerance. The Kriging meta-models accurately predicted the optimal parameters. Generally, the Kriging functions predicted the calibration parameter values and target responses consistently and accurately (Rackl & Hanley, 2016). One limitation of this process, however, is that the calibration method needs a bigger set of undefined (unknown) parameters for it to be feasible.

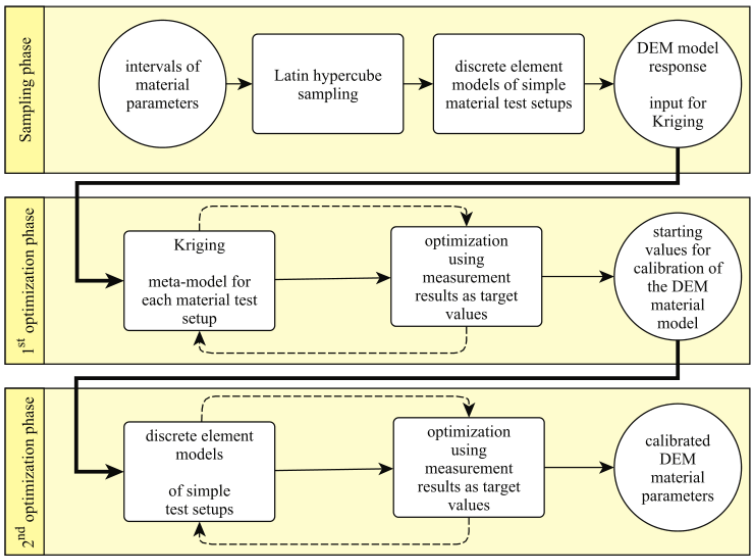

Figure 2.5: Workflow of the calibration process (Rackl & Hanley, 2017).

Another calibration method for material parameters using DEM was described by Roessler and Katterfeld (2016). The authors presented a method on the scalability of AoR tests for the calibration of DEM parameters. The lifting cylinder technique was used to determine the AoR.

Dry sand was used to conduct the experiments for different cylinder sizes (both height and diameter varied). For the first experimental phase, the AoR was determined based on the cylinder size. In the second experimental phase, the effect of lifting velocity was examined. For slow velocities, the pile of bulk material was formed in layers, whereas for high velocities, the bulk material flow was avalanche-like, and the pile formed with areas of higher and lower AoR. The AoR decreased with increase in lifting velocity (Roessler & Katterfeld, 2016).

For DEM simulations, the simulation of the AoR test involved generating an assembly of particles, settling the particles under gravity, and then raising the cylinder upwards with constant velocity. Particles flowed from the gap as the cylinder rose, and a pile was formed. The AoR was calculated after the particles settled again. To overcome the “gap problem” that occurred with the lifting cylinder test, the AoR was measured using a shear box test (Roessler & Katterfeld, 2016). The authors also calibrated cohesive material (wet sand) using the aforementioned lifting cylinder test and observed four distinct phases for the composition of the pile (stable pile, small cracks in pile, large cracks in pile, and finally static pile). A strong correlation was observed between the experimental test and the four stages of the calibration simulation. The authors showed that the lifting cylinder test provided invariant AoR results for very slow velocities only. The shear box test provided invariant AoR results much faster than the lifting cylinder method. They concluded that, despite the velocity problem, the lifting cylinder method can be used to calibrate cohesive material.

Coetzee (2016) also suggested a DEM method for calibrating parameter values for crushed rock particles (up to 40 mm) using a large shear box. The authors used two methods to form clumped particles: an optimised process and a manual process. The AoR was used to calibrate the particle-particle friction coefficient and compared with the results of the shear test. Validation of the calibration method was done by modelling anchor pull-out tests and hopper discharge for different clump types. The researchers found that even though the AoR was predicted precisely, caution was needed when using the AoR to calibrate particle-particle

friction coefficients, as it can result in a very low friction value for other applications (Coetzee, 2016).

2.4.2 Modelling of compacted material

Compaction of powdered materials is a processing method with numerous industrial applications (James, 1991; Kadir et al., 2005). Numerical simulation is a desirable technique for analysing and optimizing compaction operations. According to Garner et al. (2018), DEM is the only presently available method that can accurately simulate the powder compaction problem at particle level.

Several studies have used DEM to model compacted material. Garner et al. (2018) used DEM to study the die compaction of powders to high relative densities. The study presents a novel approach to DEM that offers a new law of force displacement which, although approximate, is more practical at high densities. The material used to calibrate the suggested DEM model parameters were milled granules of hot-melt extruded copovidone powder (Garner et al., 2018). Tablets 10 mm in diameter were compacted using a compaction simulator (Huxley Bertram) with an instrumented die. Figure 2.6 shows the DEM simulation of various compaction stages and the tensile testing of spherical particles used. For the simulation of the process of compaction, the die walls and punches were modelled as rigid, frictionless surfaces. Tensile test simulations were conducted to evaluate the strength of the assembly of the ejected pressed powder. Instead of diametral compression tests, axial tension test simulations were performed.

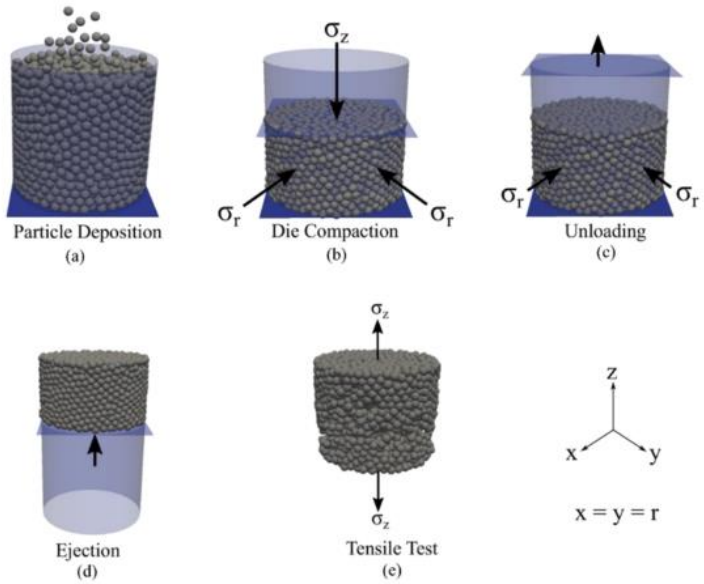

Figure 2.6: Schematic of the various stages of the compaction process and tensile testing of monosized assemblies of spherical particles simulated in DEM (Garner et al., 2018).

The DEM simulations were executed using factor level settings. First, simulations related to loading, unloading, ejection, and tensile strength were performed to attain input parameters. Response variables were calculated and optimum parameters that best fit the experimental results were obtained using an optimization procedure. Using the proposed contact model, the response surface results matched well with the DEM responses. Despite the slight deviations, the DEM results matched well with the experimental results for radial and axial stress. According to the authors, non-linearity was observed in unloading, and this was a sign of inelastic phenomena resulting from microcracking. The formation of such microcracks can lead to a partial radial wall stress relief due to linear elastic loading. The DEM approach provides better predictions, unlike the FEM models, which overpredict the residual wall stress. Strong agreement was also observed between the experimental results and the model for radial and axial stresses. However, the model underpredicted the actual level of residual wall stress and axial springback. One limitation of the calibration procedure was that very many runs were needed to attain the correct parameters for the suggested contact model.

DEM modelling of compacted material was also performed by Ransing et al. (2000), who offered a discrete and continuum modelling approach to powder compaction. Their study examined brittle and ductile particles. A von Mises yield criterion was used for ductile particles, while for brittle particles, a Rankine failure criterion was used. The calculation procedure alternated between discrete models that focused on kinetic behaviour and non-linear failure. The two calculation techniques were demonstrated across four case studies. For the DEM, the models were two dimensional and represented an assembly of rods. In the first case, the assembly involved densely packing round rods in a rigid die. At close to maximum capacity, the rods deformed and developed a simple hexagonal matrix. The calculation was compared to ductile porous material compression. The results were similar, confirming that the discrete model was able to represent the compression of a ductile assembly. The second case involved an assembly of both brittle and ductile rods. The brittle rods were mapped via triangular elements and the ductile rods by quadrilateral elements. The calculations showed that the discrete method can represent the particulate system compression. However, it is nevertheless impractical to use for modelling the compression of engineering components due to computing demands.

For continuum models, the compaction of a multilevel iron powder part and a single-level shaped ceramic part were modelled. The former aimed to attain close to uniform density in the part while, for the latter, significant density differences were unavoidable. The multilevel part represented a synchroniser hub component and was compacted by several punch motions. The density was determined using an Archimedean test. The density gradients were significant and influenced mainly by the high friction coefficient level that was used. The second model represented a ceramic tip compacted in a die between an upper and lower punch set. The compaction resulted in great density variations, and the results showed strong agreement in the form of density distribution. The authors confirmed that the discrete model could represent the compaction of an assembly of powder particles. However, due to the

computation demand of the method, it is impractical to use it for modelling the compression of a large assembly of particles.

Yan et al. (2009) also successfully used DEM to simulate the behaviour of typical granular material in the plane-strain compression mode. The authors' numerical method had the advantage of modelling granular assembly mechanical behaviour at both micro and macro levels.

2.5 Summary

The discrete element method is one of the most effective procedures used to model density distribution of the media used in shaped charges, and is the preferred method by modellers and engineers. It facilitates the maintenance of optimal performance of the devices.The literature studies in this section provided empirical evidence of the applicability of the discrete element method to predict crucial parameters in shaped charge to guarantee the said deliverables. As a matter of fact, the DEM simulation process can even model high compacting materials with extremely accurate results, which facilitates the manufacture of components that can support extremely large loads. Generally, the discrete element method is a viable and accurate methodology for predicting the parameters of the media used in a shaped charge.

This chapter provided a detailed review of literature on the applicability of DEM and FEM for modelling. In next chapter, the governing equations of the discrete element method are described.

CHAPTER 3: GOVERNING EQUATIONS IN DISCRETE ELEMENT METHOD

3.1 Introduction

Studying the microscopic and macroscopic characteristics of particles was once an exceedingly difficult endeavour, but with advances in technology, it is now possible to investigate a broad spectrum of particles' properties. Modelling particulate matter is a crucial first step in the task of understanding elements, and DEM provides a set of tools well suited to this purpose. Numerous attempts have been made to develop micro-macro transitions. Consequently, macroscopic relations have been derived from microscopic sample simulations to define particulate materials based on the theory of macroscopic continuum (Luding, 2008). This chapter analyses the components of DEM, starting with the laws of displacement, equations of motion, the normal contact force law, and the time integration scheme.

3.2 Laws of displacement

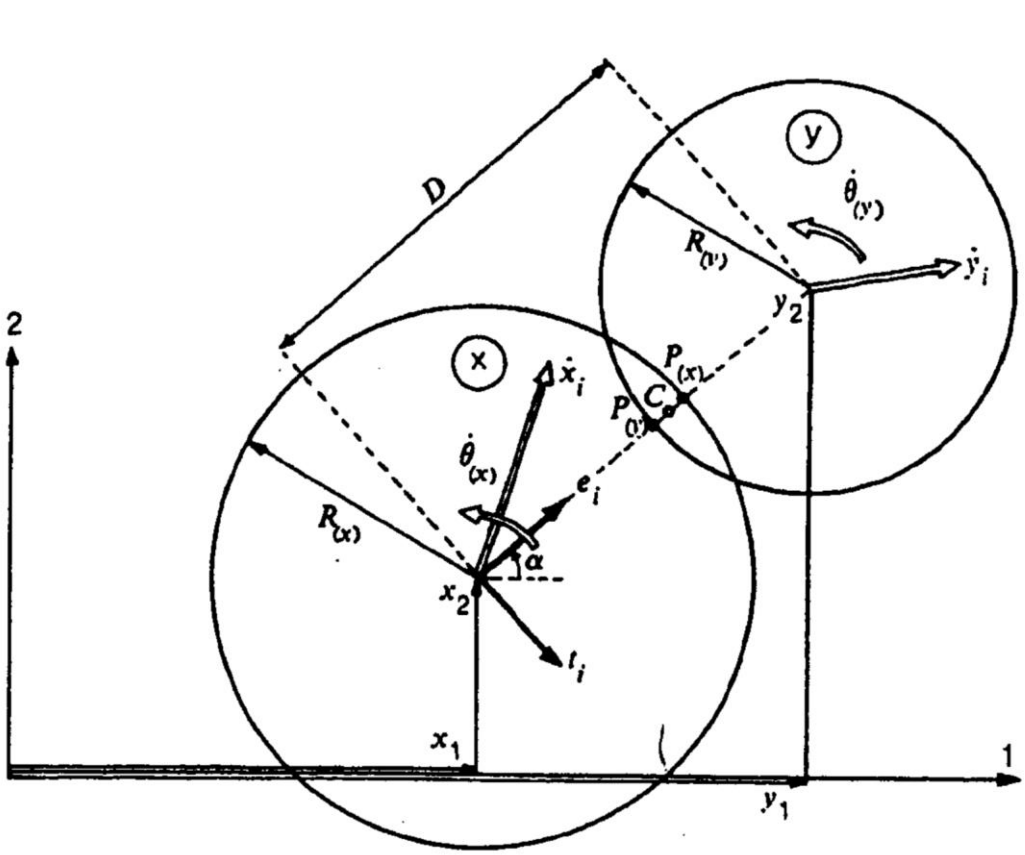

Figure 3.1: The force displacement law (Cundall & Strack, 1979)

In the two discs x and y in Figure 3.1, which are in contact, the points P_x and P_y represent the location of the intersection of a straight line connecting the two centres and boundaries (Cundall & Strack, 1979). The velocity vector components of disc x and y (respectively) are expressed as:

$$\tilde{\mathrm{x}}_{\mathrm{i}} = (\dot{\mathrm{x}}_1, \dot{\mathrm{x}}_2)$$

$$\tilde{\mathrm{y}}_{\mathrm{i}} = (\dot{\mathrm{y}}_1, \dot{\mathrm{y}}_2)$$

Furthermore, the angular velocities are positive, taken from the centre in a counter-clockwise direction and determined through differentiation with respect to time. It is worth noting that the two discs are only in contact when the sum of their radii is more than the distance between the two centres. Therefore,

$$D < R_x + R_y \tag{3.1}$$

Where D is the distance between the centres and R_x and R_y are the radii of each disc.

With this condition fulfilled, the relative velocity is integrated to determine the relative displacement during contact. Note that relative velocity is a result of velocity of the point P_x relative to P_y. The unit vector is calculated as follows:

$$e_i = \frac{y_i - x_i}{D} = (\cos\alpha \sin\alpha) \tag{3.2}$$

Additionally, e_i is rotated by 90° in a clockwise direction to produce another unit vector, t_i, expressed as follows:

$$t_i = (e_2 - e_i) \tag{3.3}$$

The relative velocity mentioned above is written as:

$$\dot{x}_i = (\dot{x}_i - \dot{y}_i) - \left(\dot{\theta}_x R_x + \dot{\theta}_y R_y\right) t_i \tag{3.4}$$

The relative velocities' normal (n) and tangential (s) components are expressed as:

$$\dot{n} = \dot{x}_i e_i = (\dot{x}_i - \dot{y}_i) e_i - \left(\dot{\theta}_x R_x + \dot{\theta}_y R_y\right) t_i e_i = (\dot{x}_i - \dot{y}_i) e_i \tag{3.5}$$

$$\dot{s} = \dot{x}_i t_i = (\dot{x}_i - \dot{y}_i) t_i - \left(\dot{\theta}_x R_x + \dot{\theta}_y R_y\right) t_i t_i = (\dot{x}_i - \dot{y}_i) t_i - \left(\dot{\theta}_x R_x + \dot{\theta}_y R_y\right) \tag{3.6}$$

The components of relative displacement increment Δs and Δn are derived from the Einstein summation convention adopted over index i and the integration of the component of relative velocity relative to time according to the equations below.

$$\Delta s = (\dot{s})\Delta t = \left\{(\dot{x}_i - \dot{y}_i) t_i - \left(\dot{\theta}_x R_x + \dot{\theta}_y R_y\right)\right\}\Delta t \tag{3.7}$$

$$\Delta n = (\dot{n})\Delta t = \{(\dot{x}_i - \dot{y}_i) e_i\}\Delta t \tag{3.8}$$

The parameters above are applied in a force-displacement law computation of normal and shear force increments, ΔF_n and ΔF_s as follows:

$$\Delta F_s = k_s \Delta s = k_s\{(\dot{x}_i - \dot{y}_i)t_i - (\dot{\theta}_x R_x + \dot{\theta}_y R_y)\}\Delta t \quad (3.9)$$

$$\Delta F_n = k_n \Delta n = k_n\{(\dot{x}_i - \dot{y}_i)e_i\}\Delta t \quad (3.10)$$

In the equations above, the coefficients k_s and k_n represent shear and normal stiffness respectively. Ultimately, the force increments are sequentially added to the sums of all force increments at each time step. Therefore,

$$(F_n)_N = (F_n)_{N-1} + \Delta F_n; (F_s)_N = (F_s)_{N-1} + \Delta F_s \quad (3.11)$$

Where N and $N-1$ represent consecutive times and, hence, $\Delta t = t_N - t_{N-1}$.

Figure 3.2 below shows a disc x and the sign typology when shear and normal forces are imminent.

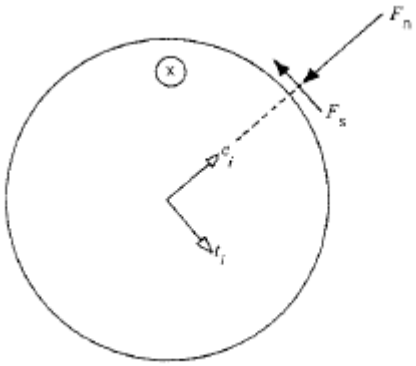

Figure 3.2: Sign convention (Cundall & Strack, 1979)

Finally, after determining both forces for each contact, the results are translated to components in directions one and two. The resultant forces denoted by $\sum F_{x1}$ and $\sum F_{x2}$ are computed as a sum of the contact force components. Note that the resultant moments (for instance, those acting on x) are considered positive when acting in the counter-clockwise direction and are calculated as:

$$\sum M_x = \sum F_s R_s \tag{3.12}$$

From the parameter above, both resultant forces and moments are used to calculate accelerations $\ddot{x}_i$ and $\ddot{\theta}_x$ based on Newton's second law of motion.

3.3 Equations of motion

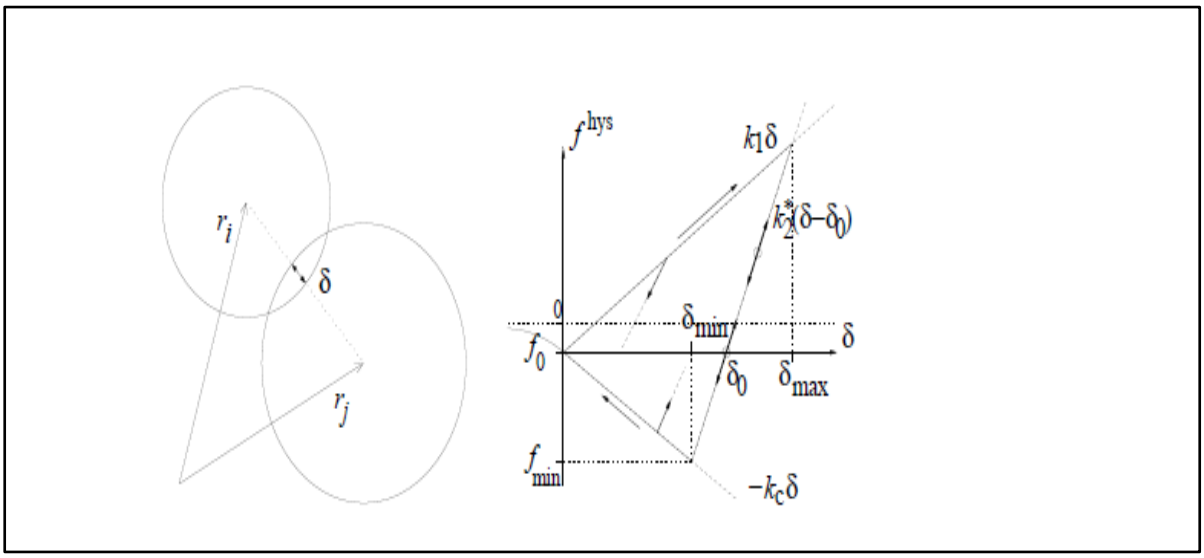

Figure 3.3: Discs r and j in contact with overlap and all the other parameters shown (Luding, 2008)

The fundamental units of particulate materials, which are known as mesoscopic grains, normally undergo deformation under stress. As mentioned previously, it is difficult to produce the actual deformation model, hence the overlap δ related to the interaction force (as shown in Figure 3.3). The total forces f_i on the first particle (i) originate from either external forces or other particles. If the forces are known, the three motion laws described by Newton are applied for translational and rotational degrees of freedom as shown below:

$$I_i \frac{d}{dt}\omega_t = t_i \tag{3.13}$$

$$m_i \frac{d^2}{dt^2} r_i = f_i + m_i g \tag{3.14}$$

Where I is the position of the particle and m_i is the mass, and the total force acting on it due to contact with walls and other particles is $f_i = \sum_c f_i^c$. Additionally, the particle gains acceleration as a result of forces such as gravity g, and I_i represents the moment of inertia for the spherical particle, while ω_t is the angular velocity. Finally, $t_t = \sum_c (l_i^c x\, f_i^c + q_i^c)$ is the total Torque. It is worth mentioning that the torque/couples q_i^c occur at the contacts as a result of torsion and rolling.

Motion expressions are typically a series of ordinary differential equations in the form of D+D(D-1)/2, which are coupled and manipulated in dimensions of D. According to Luding (2008), solving equations of motion is possible through numerical integration tools presented by numerous researchers in the past. Short-ranged and long-ranged interactions of particulate materials are analysed using linked-cell techniques and other methods, although short-ranged cases are easier to solve. Furthermore, long-ranged interactions include those that occur in space and Coloumb interactions.

3.4 Normal contact force laws

The two categories of normal contact force law models are linear and adhesive elasto-plastic normal contact models, and they are described in detail in the following sections.

3.4.1 Linear normal contact model

The spherical particles shown in Figure 3.3 above can only interact when their overlap is:

$$\delta = \left(a_i + a_j\right) - (r_i - r_i) \cdot n \qquad (3.15)$$

where a_i and a_j are the respective radii. The difference between r and a is that a is the radius of the undeformed particle whereas r is the actual raduis between the center point and the deformed particle surface.

The following conditions hold:

The overlap should be positive, meaning $\delta > 0$, and the unit vector denoted by *n* points from *j* to *i* is calculated as:

$$n = n_{ij} = (r_i - r_j)/|r_i - r_j| \tag{3.16}$$

Upon contact, the force imposed on a particle *i* from a second element *j* is broken down to normal and tangential components, as illustrated below:

$$f^c = f_i^c = f^n n + f^t t \tag{3.17}$$

The normal contact force takes into consideration linear dissipative and repulsive forces, and involves energy dissipation due to internal fraction or any other means by which energy is absorbed and volume is displaced by the particle.

$$f^n = k\delta + \gamma_0 \mu_n \tag{3.18}$$

γ_0 is the viscous damping coefficient, and k is the spring stiffness.

The relative velocity following the normal direction $\mu_n = -\mu_{ij} \cdot n = -(\mu_i - \mu_j).n = \delta^0$. This so-called linear spring dashpot model allows to view the particle contact as a damped harmonic oscillator, for which the half-period of a vibration around an equilibrium position, see Fig. 1, can be computed, and the typical response time on the contact level is calculated as:

$$t_c = \frac{\pi}{\omega} \text{ whereby } \omega(\text{eigenfrequency}) = \sqrt{(k/m_{12}) - \eta_0^2} \tag{3.19}$$

The damping coefficient $\eta_0 = \gamma_0/(2m_{ij})$ where $m_{ij}(\text{reduced mass}) = m_i m_j/(m_i + m_j)$

The coefficient of restitution

$$r = -\frac{v_n'}{v_n} = \exp\left(-\frac{\pi\eta_0}{\omega}\right) = \exp(-\eta_0 t_c) \tag{3.20}$$

The coefficient determines the magnitude of relative velocity ratio before and after the collision of the particles (Luding, 2008).

3.4.2 Adhesive, elasto-plastic normal contact model

In this case, the linear hysteric spring model is used. This implies that plastic deformations take place at the point of contact. Equations (3.20-3.22) below represents all the hysteresis forces involved.

$$f^{\text{hys}} = \begin{cases} k_1\delta & \text{for loading,} \quad \text{if } k_2^*(\delta - \delta_0) \geq k_1\delta & (3.21) \\ k_2^*(\delta - \delta_0) & \text{for un reloading,} \quad \text{if } k_1\delta > k_2^*(\delta - \delta_0) > -k_c\delta & (3.22) \\ -k_c\delta & \text{for unloading,} \quad \text{if } -k_c\delta \geq k_2^*(\delta - \delta_0) & (3.23) \end{cases}$$

When loading commences, overlap and forces have a direct linear relationship up to the instant when maximum overlap is attained. Conversely, during the unloading phase,the force falls from its point at δ_{max} to zero at $\delta_0 = (1 - k_1/k_2^*)\delta_{max}$. Additionally, k_1 and k_2 are slopes of respective plots, and reloading the force increases following k_2 until maximum force is attained (Luding, 2008). However, a further increase in the overlap follows k_1 once more, and, as a result, the maximum overlap should be adjusted.

When loading occurs below δ_0 , negative inattractive forces develop up to the instant where minimum force, expressed as $-k_c\delta_{min}$, is attained. Therefore, the minimum overlap is computed as:

$$\delta_{min} = (k_2^* - k_1)\delta_{max}/(k_2^* + k_c) \quad (3.24)$$

Finally, any further unloading converts the minimum force to attractive forces located at the adhesive branch and expressed as $f^{hys} = -k_c\delta$. The maxium attractive forces that can be attained occur when k_c approaches infinity and, hence, the following results:

$$f_{max}^{hys} = -(k_2 - k_1)\delta_{max} \quad (3.25)$$

3.5 Time integration schemes

Equations of motion in DEM can be solved in multiple ways, but time integration schemes have proven to be the most effective (Kruggel-Emden, Sturm, Wirtz & Scherer, 2008). Time integration systems are categorised as either implicit or explicit. The former assume that the effectiveness of a matrix ought to be factorised, whereas the latter do not adhere to this rule (Nam & Choi, 2017). It is also imperative to note that, owing to the individual characteristics of each scheme, either method is chosen depending on the nature of application.

Compared to explicit integration systems, implicit integration systems involve more intense computation at each instant. However, the former achieves high parallel efficiency while requiring minimum communication between processors (Noh & Bathe, 2013). Additionally, implicit schemes can be customised to perform linear analysis so that unconditional stability is attained and the size of the time step is selected only based on the properties of the problem. Conversely, explicit time integration schemes are simple, and they achieve high rates of efficiency during paralleling. These systems only require vector calculations when applying diagonal matrices and, hence, their cost per time is low. Nevertheless, explicit schemes achieve only conditional stability. It is therefore imperative that explicit time integration systems are suited for situations where the size of the time step required to attain specific stability is approximately equal to the same parameter required for describing the physical problem.

3.6 Summary

Discrete element method involves a range of laws and equations used to analyse particulate materials. The laws of displacement determine the expressions required to caclulate parameters such as degrees of freedom and total forces. Similarly, the laws of motion describe the motion of the particles relative to each other, while time integration schemes solve equations of motion. Overall, the discrete element analysis of particulate materials is an

overarching approach that should be embraced on a wide scope. In the following chapter, the material calibration methodology is described.

CHAPTER 4: CALIBRATION OF MATERIAL PARAMETERS

4.1 Introduction

The applications of DEM in industry for the purposes of handling bulk materials, processing, and modelling are growing. A particular emphasis has been placed on material parameters calibration and the uses of computer resources in conducting these operations. A DEM model incorporates the inertial properties of the material (such as size, shape, and density), its mechanical properties such as stiffness, and the interaction between the material and other objects such as boundary conditions. This chapter describes the experimental procedure for the calibration of material parameters. This is followed by the numerical replication of the experiment by means of DEM. The experimental results were compared to the DEM results to determine the accuracy of the numerical model.

4.2 Particle size and shape distribution

Owing to time constraints and the unavailability of sophisticated techniques like the use of a scanning electron microscope, visual inspection was used to determine the particle shape and size distribution. The particle shape was classified using three general shape identifiers based on visual inspection, which is a suitable approach in this study.

The following approach was used to estimate particle size and shape distributions. First, three random samples of particles were taken from the bulk of PBX material, such that each sample contained three particles. The samples were representative of the bulk, and it was assumed that the whole bulk had the same dimensions and shape. Visual inspection was used to estimate the shape of the particles, and their dimensions. Three shapes were identified from the random samples, and, for the sake of simplicity, these shapes were assumed to be the only shapes represented in the bulk of PBX material.

All particles in the random sample were categorised into three shapes based on their appearances. The shapes identified using visual inspection were identified in the simulation

as having a faceted shape, a rounded cylinder shape, or a spherical shape, as seen in Figures 4.2, 4.3, and 4.4. Figure 4.1 shows the representative sample of the PBX bulk material. The dimensions of the sieve size of the particles were estimated using a ruler. The estimations for the shapes were as follows: (a) the small particles identified as having a spherical shape in the DEM model had a size between 1 mm and 2 mm; (b) the medium-sized particles identified as having a round cylinder shape had a size of approximately 2 mm; (c) the large particles identified as having a faceted shape had a size of approximately 3.5 mm.

Figure 4.1: Particles of PBX

Rocky software version 4 was used, and DEM replications of the specific shapes were performed. These are shown in Figures 4.2, 4.3, and 4.4.

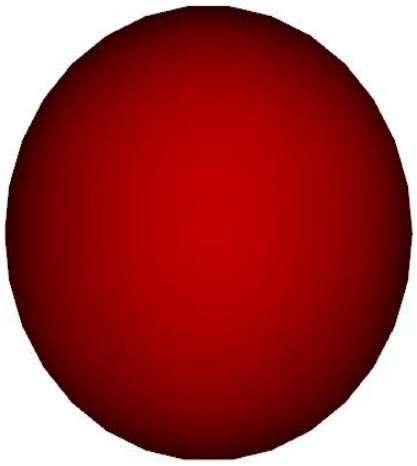

Figure 4.2: DEM equivalent for spherical shape

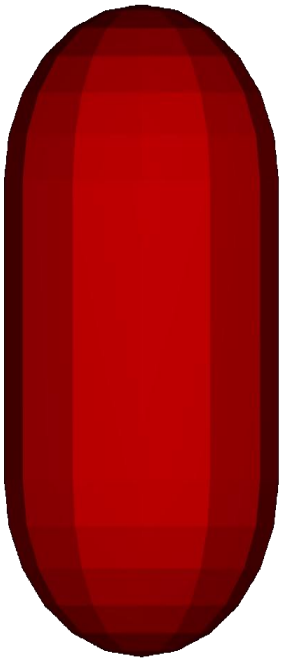

Figure 4.3: DEM equivalent for rounded cylinder shape

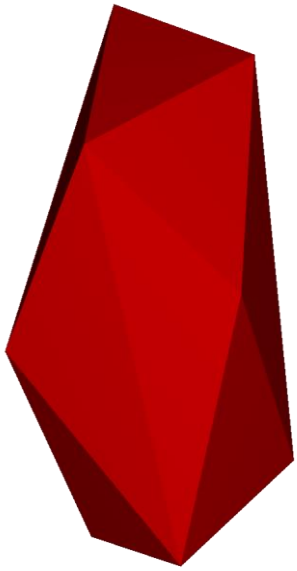

Figure 4.4: DEM equivalent for faceted shape

The occurrence of the faceted shape was estimated to be 20% of the sample, that of the rounded cylinder was estimated to be 30%, and that of the spherical shape was estimated to be 50%. These results are only meant to serve as a basic indication of the shape and size distribution of the packing from which equivalent numerical parameters were replicated in the DEM simulation. Using the classification method mentioned, size distributions detailed in Table 4.1 were obtained, which were directly implemented in the DEM software.

Table 4.1: Results for shape and size distribution estimation

Shape	Sieve Size (mm)	Volume (%)
Faceted shape	3.50	20.00
Rounded cylinder	2.00	30.00
Spherical shape	1.00 and 2.00	50.00

4.3 Measuring bulk density and angle of repose

The bulk density can generally be defined as the mass of a bulk material sample divided by the bulk volume that the sample occupies (Head, 1989). This is different from particle density,

as bulk volume is different for a large quantity of particles due to shape and air entrapment. Bulk volume includes all voids and gaps between particles as shown in Figure 4.5. Here, V_b refers to bulk volume, V_s refers to volume of solid, and V_v is the volume of voids.

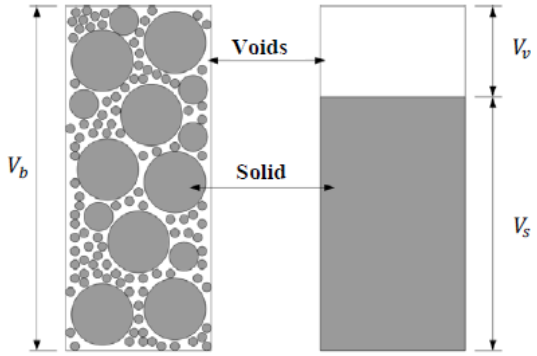

Figure 4.5: Bulk volume, voids volume and, solid volume (Head, 1989)

To measure bulk density, a container of specific shape (such as a rectangular prism) is filled completely with a known mass of the material up to a predetermined height. The mass of the bulk material that is placed in the container is represented as m_b. The height to which the container is filled is the volume V_b. The method for calculating V_b for a rectangular prism-shaped container is shown in Equation 4.1.

$$V_b = l \times w \times h \tag{4.1}$$

Where l refers to length of container, w refers to its width, and h refers to the height to which material has been filled in the container. Together, m_b and V_b are used to obtain bulk density ρ_b as shown in Equation 4.2.

$$\rho_b = \frac{m_b}{V_b} \tag{4.2}$$

If desired, the void ratio can be calculated as shown in Equation 4.3.

$$e = \frac{V_v}{V_s} \tag{4.3}$$

Where e refers to the void ratio. The Void ratio is closely related to the porosity if porosity is expressed as ratio.

$$n = \frac{e}{1+e} \quad (4.4)$$

and

$$e = \frac{n}{1-n} \quad (4.5)$$

The porosity ratio can be calculated from the bulk density and the particle density as shown in Equation

$$n = (1 - \frac{\rho_b}{\rho_m}) \quad (4.6)$$

The total solid volume can be determined by placing a known volume of water in the container and then placing the bulk material into the water. The volume that is displaced is the total solid volume. In this project, the water displacement method was not used because the actual density of the PBX material was used in the DEM simulation.

The experimental procedure adopted to measure the bulk density for the PBX material involved the use of a rectangular container as shown in Figure 4.7. The container dimensions were 10 cm × 10 cm × 2.5 cm. The container was filled with the bulk material, and then levelled using a ruler to give a uniform surface as shown in Figure 4.8. There was some mild spillage of material that overflowed the top of the container, but this was neglected, as it did not affect the end results obtained. The material was then unloaded from the box so that it formed a pile, as shown in Figure 4.9. After that, the AoR was measured manually by visual inspection. This involved placing a sheet marked with 1cm × 1cm squares behind the pile as shown in Figure 4.9. Finally, the mass of the bulk material was weighed, as shown in Figure 4.10 and the void ratio and porosity was calculated by using Equation 4.5 and 4.6. This experiment was repeated three times. Table 4.2 summarises the results of the experiment and the calculations.

Table 4.2: Bulk properties (experimental).

	Run 1	Run 2	Run 3	Average	RDM Lab
Total mass (g)	208.30	209.20	207.70	208.40	258.39
Bulk volume (cm^3)	250.00	250.00	250.00	250.00	319.32
Bulk density (kg/m^3)	833.20	836.80	830.80	833.60	809.00
Porosity (%)	37.00	37.00	37.00	37.00	39.00
Void ratio	0.59	0.59	0.59	0.59	0.64
AoR	31°	32°	30°	31°	

The variation between the experimental bulk density and the lab result is 3%. However, the RDM lab results were used to verify the DEM result. The angle of repose in the three experiments ranged between 30° and 32°.The average AoR of 31° was used to calibrate the DEM angle of repose. Image processing technology is recommended for future work to measure the experimental AoR accurately.

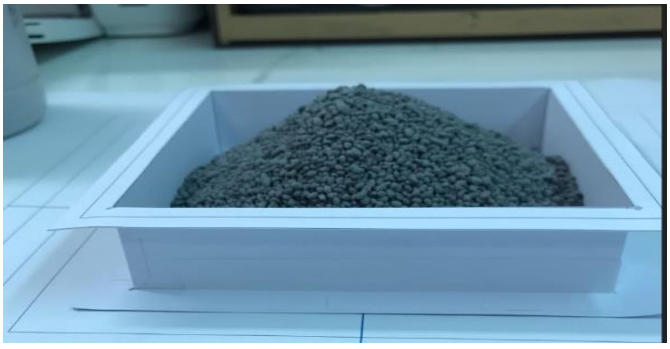

Figure 4.6: Bulk material piled in container

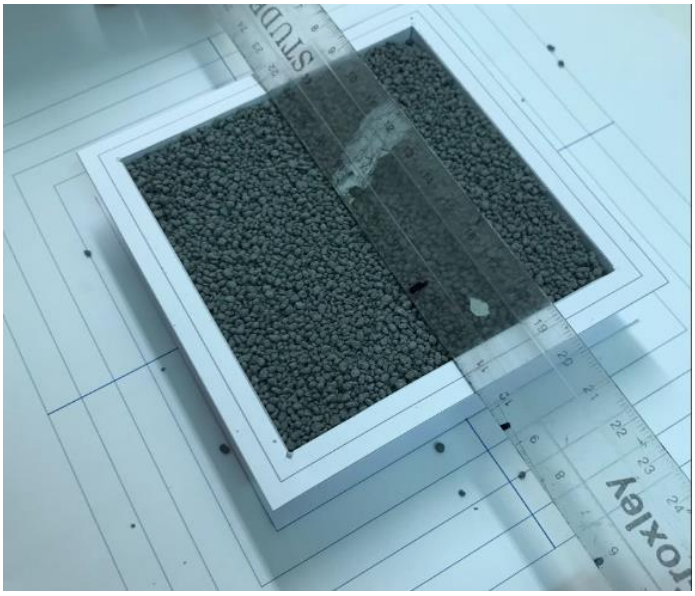

Figure 4.7: Bulk material levelled in the container

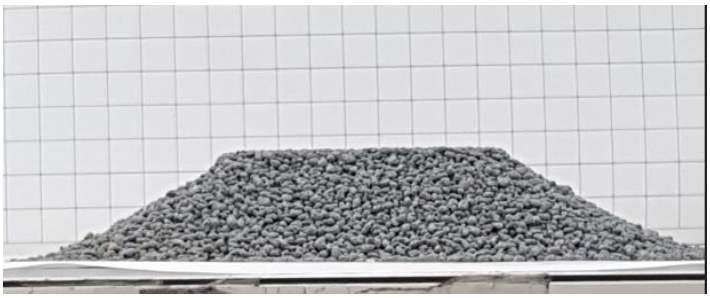

Figure 4.8: Pile formed for AoR measurement

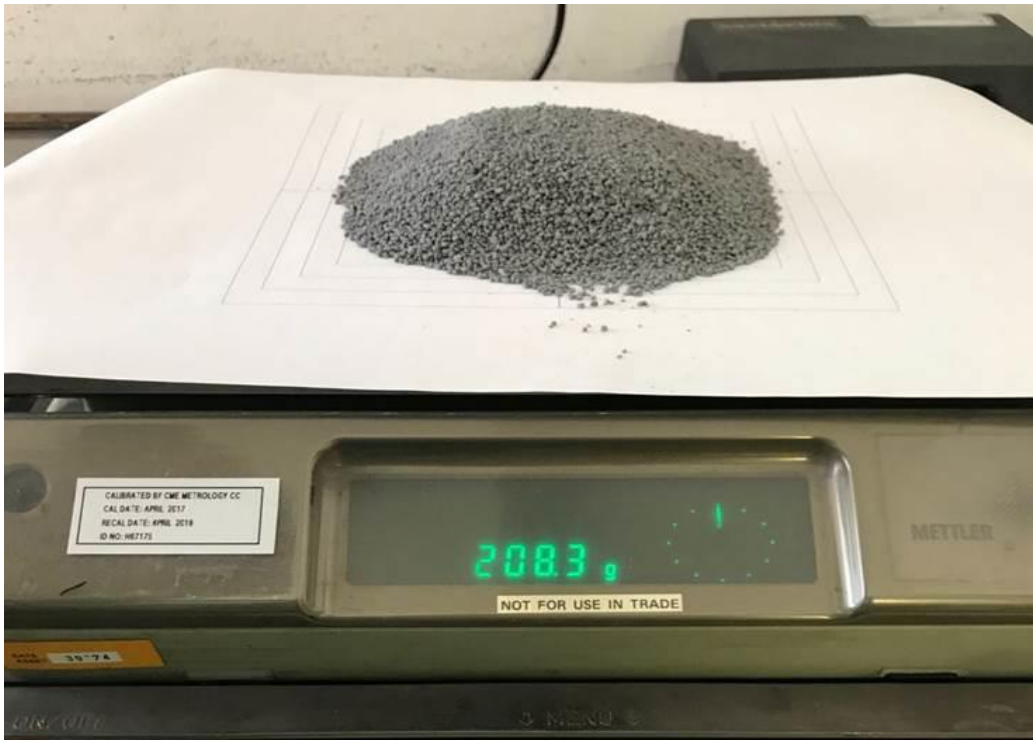

Figure 4.9: The mass of the bulk material used in the experiment.

4.4 Numerical work

A DEM simulation was used to replicate the experimental procedure mentioned above. The AoR test was performed to calibrate the static friction coefficient and bulk density.

4.4.1 DEM parameter used for simulation

The accuracy of the results of the DEM simulation are largely dependent on the input parameters (Coetzee, 2017). Certain parameters were obtained from the RDM lab, while other parameters were calibrated manually, including the particle-particle friction coefficient. It was assumed that the particle-wall coefficient of friction contributed an insignificant effect in terms of the simulation's end result. Thus, a default value from Rocky was used for the particle-wall coefficient of friction which was 0.30. Additionally, rolling friction was not taken into consideration since the particles were not fully spherical.

Generating particles was the first step in DEM that used data from the real-life sample. The particle shape and distribution were specified according to an estimation of the visual inspection described in section 4.2. The particle size was specified based on the sieve sizes given in Table 4.1.

Table 4.3 shows the value of the parameters used in the simulation, which remained unchanged for the calibration tests.

Table 4.3: PBX Property obtained from RDM.

Particle density	1322 kg/m^3
Young's modulus	1 Gpa
Poisson's ratio	0.35

4.4.2 Calibration of Particle-Particle friction (static friction coefficient)

The static friction coefficient plays a primary role in determining AoR (Yan, Wilkinson, Stitt, & Marigo, 2015). For this reason, the AoR test was performed to calibrate the static friction. The first step was estimating a value for the friction coefficient. The second step was running the simulation to determine the angle of repose, then calculating the difference between the obtained angle and the desired angle. This process was repeated iteratively until the angle nearly matched the experimental result described in section 4.3.

4.4.2.1 Angle of repose test

The experimental setup was replicated in the simulation. First, the size of the rectangular box was modelled. Then, the particle size was generated, taking into consideration material specifications such as density. Following this, the levelling action of the ruler was modelled. Finally, the upward motion the container, which caused the particles to form a pile, was modelled, and the AoR was obtained. This is illustrated in Figures 4.10, 4.11, 4.12, and 4.13. The numerical procedure strictly follows the experimental procedure described in section 4.3.

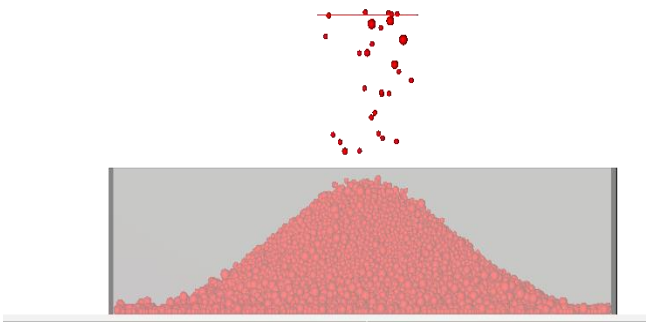

Figure 4.10: An illustration of the box-filling process.

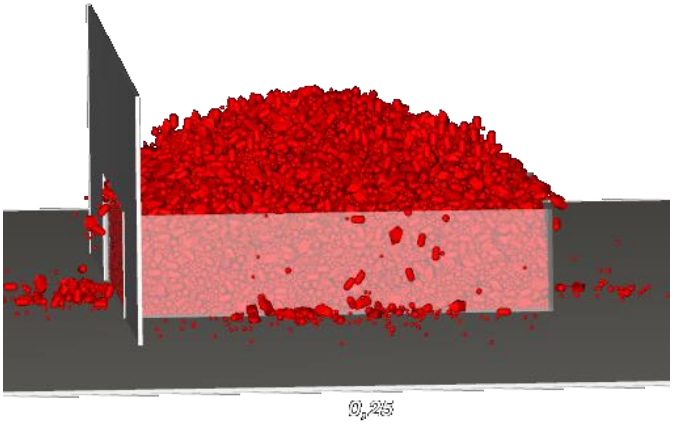

Figure 4.11: Modelling of ruler levelling action

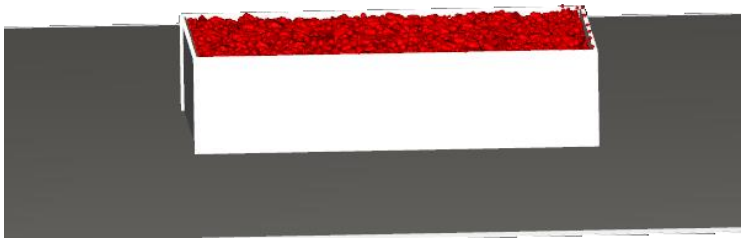

Figure 4.12: Levelled container

The simulation was repeated as the static friction coefficient was adjusted, and the resulting AoR was measured. To measure the numerical AoR, the simulation result was exported to an Excel file, which was used to formulate a line based on the position of particles as shown in Figure 4.13. Table 4.4 represents the static friction coefficient and resulting angle of repose.

Table 4.4: Static friction coefficient and resulting numerical AoR

Static friction coefficient	0.30	0.45	0.50	0.58
Angle of Repose	17°	24°	27°	30°

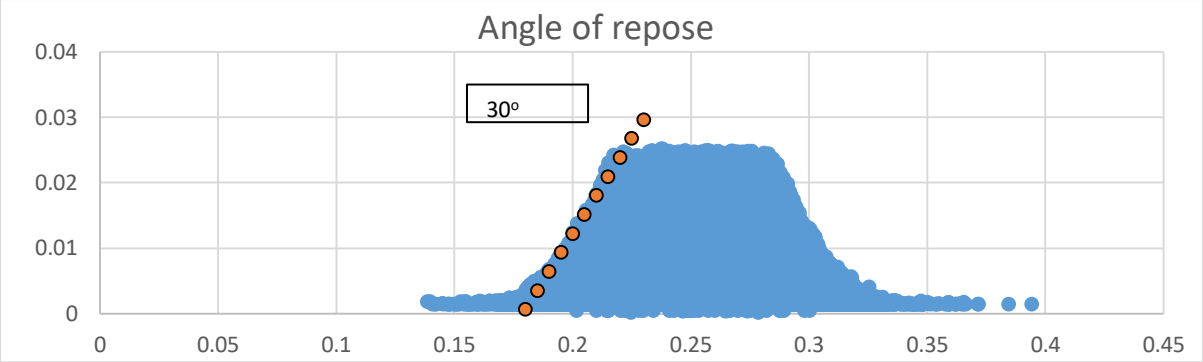

Figure 4.13: The DEM simulation AoR at static friction of 0.58 after extracting the result to Excel file.

The data in Table 4.4 demonstrate that the static friction plays a primary role in determining AoR. The friction coefficient of 0.58 resulted in an AoR of 30°, which is close to the experimental result of 31°.

4.5 Comparison between experimental and numerical results

After the static friction coefficient was calibrated to produce a value closest to the desired angle of repose, the simulation was stopped and the result was recorded. Table 4.5 presents a comparison of bulk properties between the DEM and experimental results.

Table 4.5: Comparison of DEM and experimental bulk properties

Parameter	**DEM**	**Experimental**	**Variation (%)**
Total mass (g)	203.10	208.30	2.50
Bulk Volume cm^3	250.00	250.00	0.00
Bulk density(kg/m^3)	812.46	809.00	0.42
Porosity (%)	39.00	37.00	2.00
Void ratio	0.61	0.59	3.4

AoR	31	30	3.3

The simulation result for the mass of the PBX material was 203.11 g, whereas the experimental result was 208.30 g for the same volume. The total difference in mass amounts to 5.20 g. The RDM lab report bulk density was 809 kg/m^3, whereas the simulation result was 812.46 kg/m^3. The variation in the bulk density was only 0.42%. The numerical AoR was 30° while the experimental angle of repose was 31°, a difference of only one degree. The variation among the bulk properties ranged between 0.42% and 3.40%.

4.6 Summary

The purpose of this experiment was to calibrate the static friction coefficient and verify the input parameters for PBX material granulated particles. Random sampling was done via visual inspection to estimate the shape and size distributions of PBX particles. Then, the AoR test was performed to calibrate the static friction coefficient. The AoR test was done experimentally and replicated numerically. The results obtained from the simulation were then compared to the experimental results.

Considering the relatively minor variation between the experimental and numerical bulk densities, AoR and the calibration procedure can be regarded as satisfactory.

The bulk properties that were obtained through numerical iteration, along with other properties that were obtained directly from the RDM lab, are summarised in Table 4.6.

Table 4.6: Final DEM input parameters' calibration results

Parameter		Result		
Particle shape distribution		Faceted shape	Rounded cylinder	Spherical
Particle size distribution	Sieve size (mm)	3.50	2.00	1.00
	Volume (%)	20	30	50
Particle density (kg/m^3)		1322.00		
Poisson's ratio		0.35		
Static friction coefficient		0.58		
Young's Modulus (Gpa)		1.00		

In next chapter, the simulation of the pressing process is described. The verification of the results is also discussed.

CHAPTER 5: NUMERICAL MODELLING

5.1 Introduction

This chapter discusses the modelling of the consolidation process based on the material parameter calibration results in the previous chapter. DEM was used to examine the pressing process of shaped charges, as the consolidation process involves granular interactions. The chapter describes the setup of the experimental pressing process as well as the DEM model setup, which uses the AutoCAD program. The simulation of the consolidation processes is also described, and the results discussed. An explanation of the density distribution of the particles during the pressing process with reference to the different grid sizes follows. The chapter then concludes with the verification of the results.

5.2 Developing pressing process simulation system model

The pressing process requires the setup shown in Figure 5.1. The setup consists of a casing with a diameter of 8.5 cm, which is filled with explosive charges. Top and bottom rammers enclose the casing at both ends. The pressing process occurs by forcing the top rammer to press down on the explosive material with a force of 58.5 tons. This force was specified by RDM.

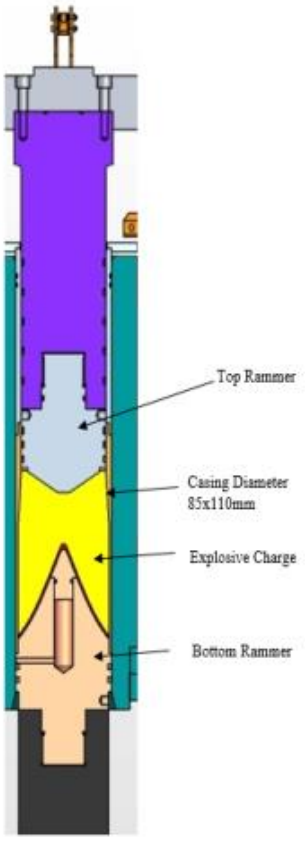

Figure 5.1: 2D cross-section of the processing press showing the top and bottom rammers and the casing in relation to the explosive charge.

5.3 DEM model setup

5.3.1 Pressing tool setup

For the DEM model, 3D geometries of the tools for the pressing process apparatus were imported from AutoCAD. These geometries are shown in Figures 5.2, 5.3, and 5.4 below. For more accurate results, care was taken to ensure that the dimensions used for the tools were those of the real tools currently in use by the company. The dimensions were provided by the plant department at RDM.

Figure 5.2: A 3D model of the bottom rammer

Figure 5.3: A 3D model of the casing

Figure 5.4: A 3D model of the top rammer

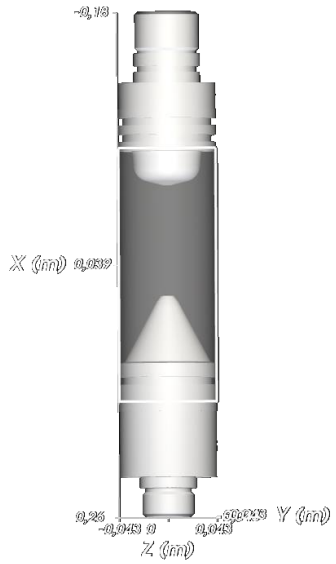

Figure 5.5: A 3D model of the pressing tool

5.3.2 Material data inputs

The material characterisation process described in Chapter 4 was used to set up the material specifications for the DEM model. The material properties and particle-particle contacts used in the simulation were the same properties used in the material calibration simulation summarised in Table 4.3. Rocky software applied a default value of 0.3 for the particle-wall coefficient of friction which was used in the simulation.

5.4 Consolidation process simulation

The simulation was carried out first by filling the casing with explosive material as shown in Figures 5.6 and 5.7. Then, the top rammer was made to move down into the casing (as shown in Figure 5.8) with a force of 58.5 tons, replicating a real-life process used by the company. There was no time limit involved in the simulation, nor any force limit. The simulation was stopped manually when the top rammer was unable to press any further into the material and the density results ceased to change.

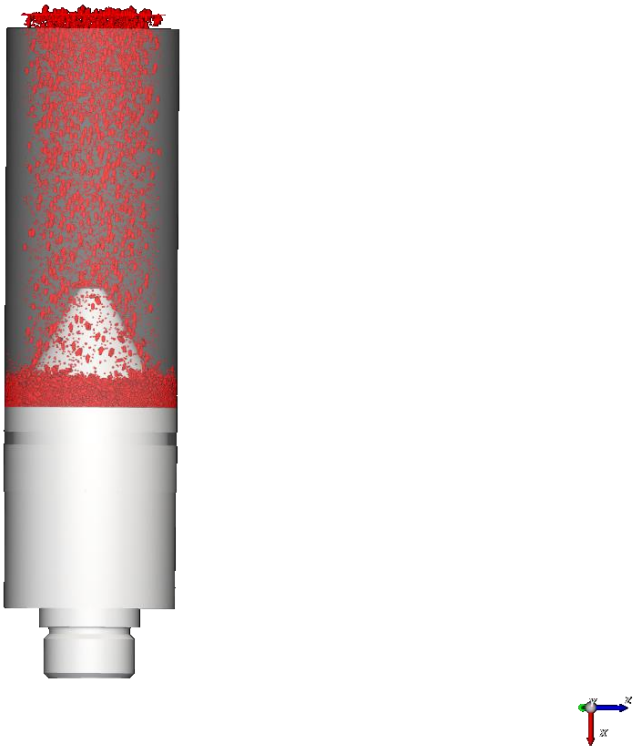

Figure 5.6: Filling the casing with particles

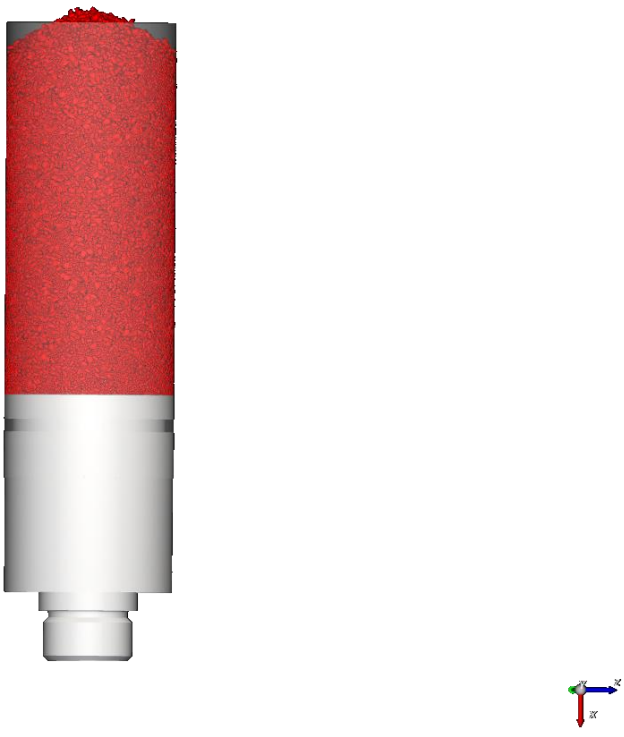

Figure 5.7: Filled casing

Figure 5.8: Top rammer moving down to press the material

5.5 Simulation results

At the moment when the top rammer could not move down any further due to resistance from the material being pressed and the simulation results had stopped changing, the simulation was stopped manually, and the cross sections of the particles were observed to determine the internal density distribution. The following sections describe the results of this analysis (and of the simulation more broadly).

5.5.1 Maximum normal force

Figure 5.9 below shows the results obtained from the DEM model. The colour scale ranges from dark blue to red. Dark blue represents the minimum force acting on the particles, whereas red represents the maximum normal force. The normal forces in the blue areas range from

0 N to 364 N. The light green to yellow colours represents medium normal force, which ranges from 364 N to 1093 N. The maximum normal forces acting on the particles occurred in the red areas.

It can be observed from Figure 5.9 that a number of particles reached a maximum normal force of approximately 1450 N, while the majority of the particles in the casing (shown in blue) experienced a maximum normal force of about 364 N. It This difference of about five times is due to the size of the particles. It can be observed from Figure 5.9 that as the particle size increases, so too does the magnitude of the maximum normal force. In static packing, the average maximal normal force scales linearly with the average particle radius (Torok, Unger, Fazekas & Wolf, 2005).

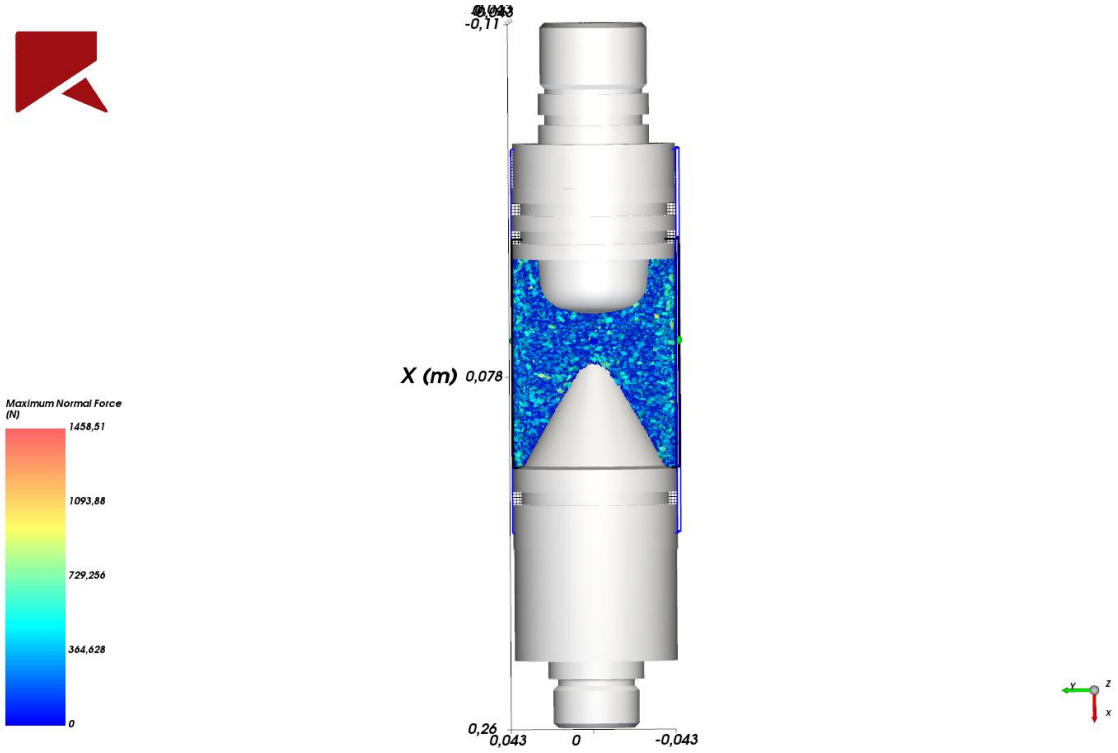

Figure 5.9: Maximum normal force distribution on particles in the casing

5.5.2 Density distribution

A three dimensional cross-sections of the particles were taken to observe the inside density distribution of the material in the casing during the pressing process, with the dimensions of

each cross section being 150 mm x 86 mm x 60 mm. Following this, three different grid sizes were generated to observe the effectiveness of various grid sizes in the simulation result. The following sections show the results of density variations under different grid sizes.

5.5.2.1 Fine grid size

The first grid size generated was fine. Each grid square was 1.17 mm x 0.67 mm. This grid size was chosen because it is closest to approximating the sensor width of the CT scan.

This grid size produced the density distribution spectrum shown in Figure 5.10. In Figure 5.10, the colour scale represents the density in kg/m^3. Blue represents the low-density distribution, with a maximum density of 380 kg/m^3. The light green to yellow colour represents the medium-density region, which ranges from 380 kg/m^3 to 1080 kg/m^3. The high-density distribution ranges from 1080 kg/m^3 to 1400 kg/m^3 and represented are by the red colour.

These figures depict a high-density area in the central region of the casing between the top and bottom rammers. Here, the density reached a peak of 1400 kg/m^3, as shown in red. On the other hand, regions close to the wall and base of the bottom rammer experienced a medium density of about 400 kg/m^3, as shown in green. The results with uneven density distributions indicate that these regions closer to the wall were mostly unaffected by the pressing process, and therefore highlight a weakness of the conventional pressing process.

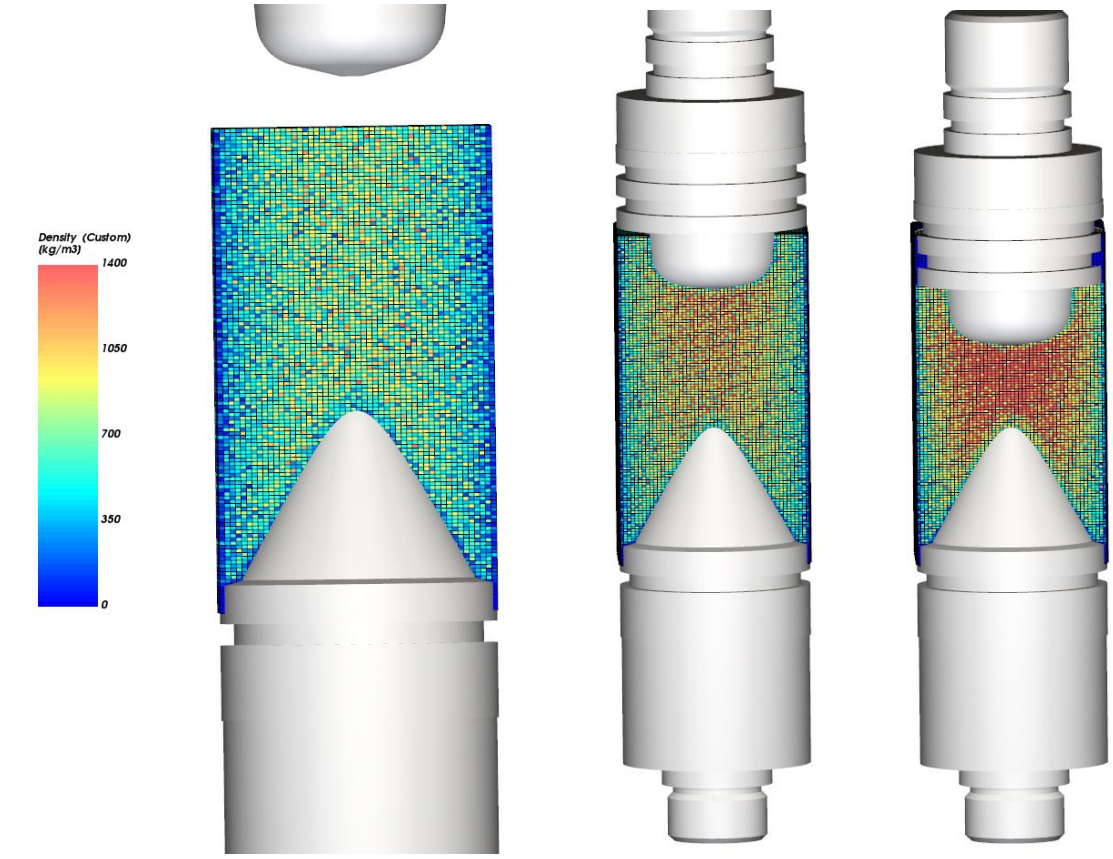

,

Figure 5.10: Density distribution during the pressing process (grid size is 1.17 mm x 0.67 mm)

In Figure 5.10, while the top rammer is moving, the density in the casing ranges between blue and yellow, with red almost not appearing at all. This indicates low density in areas close to the edges and around the bottom rammer (i.e., less than 350 kg/m^3) and medium density in the areas between the top and bottom rammer (i.e., 350 kg/m^3 to 1050 kg/m^3).

During the intermediate stage, low density can still be observed along the edges, but higher density occurs in the central region between the top and bottom rammers. In the central region, the density range increased to between 850 kg/m^3 and 1400 kg/m^3, compared to the earlier value of 350 kg/m^3 to 1050 kg/m^3.

The final stage, which corresponds to the moment at which rammer stopped moving and the results ceased to change, displays a high-density area in the central region of the casing

between the top and bottom rammers. Here, the density reaches a peak of 1400 kg/m^3. On the other hand, regions close to the wall and base of the bottom rammer experienced only medium density, with a maximum of 400 kg/m^3. The uneven density distribution in these results indicates that these regions closer to the wall were mostly unaffected by the pressing process.

5.5.2.2 Medium grid size

The second grid size was 3.57mm x 3.44 mm. This grid size was chosen based on the largest particle sieve size used in the model, which was 3.5mm.

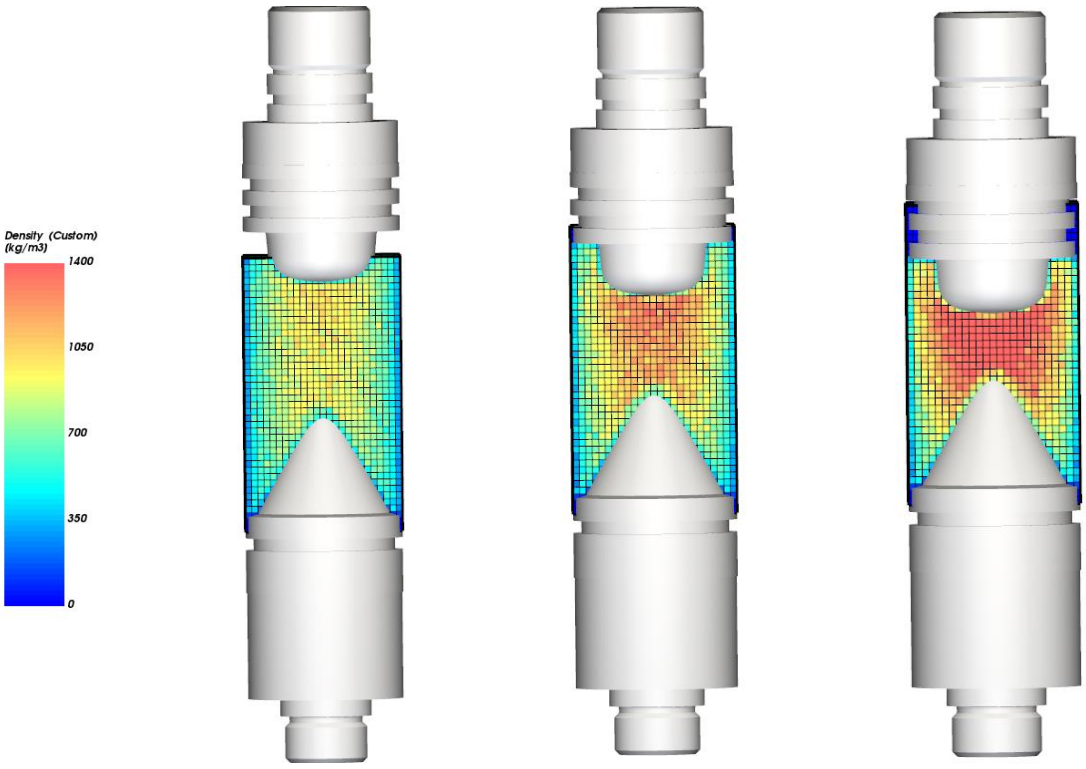

Figure 5.11: Density distribution during the pressing process (grid size is 3.57mm x 3.44 mm)

As shown in Figure 5.11, as the top rammer starts to move at the beginning of the pressing process, the density in the central region displays a higher density than the region close to the

boundaries. It ranges approximately between 700 kg/m^3 and 1050 kg/m^3, whereas the area in contact with the wall experienced a maximum density of 400 kg/m^3.

During the pressing process, the density in the central region increased comparing to the early stage of pressing. The density ranges between 1050 kg/m^3 to 1400 kg/m^3 while it slightly changed at nearing to the boundaries.

In the final stage, the density reached a peak in the central region of the casing between the top and bottom rammers. By contrast, regions close to the wall and the base of the bottom rammer experienced only medium density (with a maximum of roughly 900 kg/m^3) The regions close to the wall had the lowest overall density.

5.5.2.3 Large grid size

The final grid size chosen for the study used 7.14mm x 6.61 mm squares. This grid size was chosen to examine the results when the grid size was larger than the particle size. Figure 5.12 demonstrates the density variations in the casing during the simulation of the pressing process.

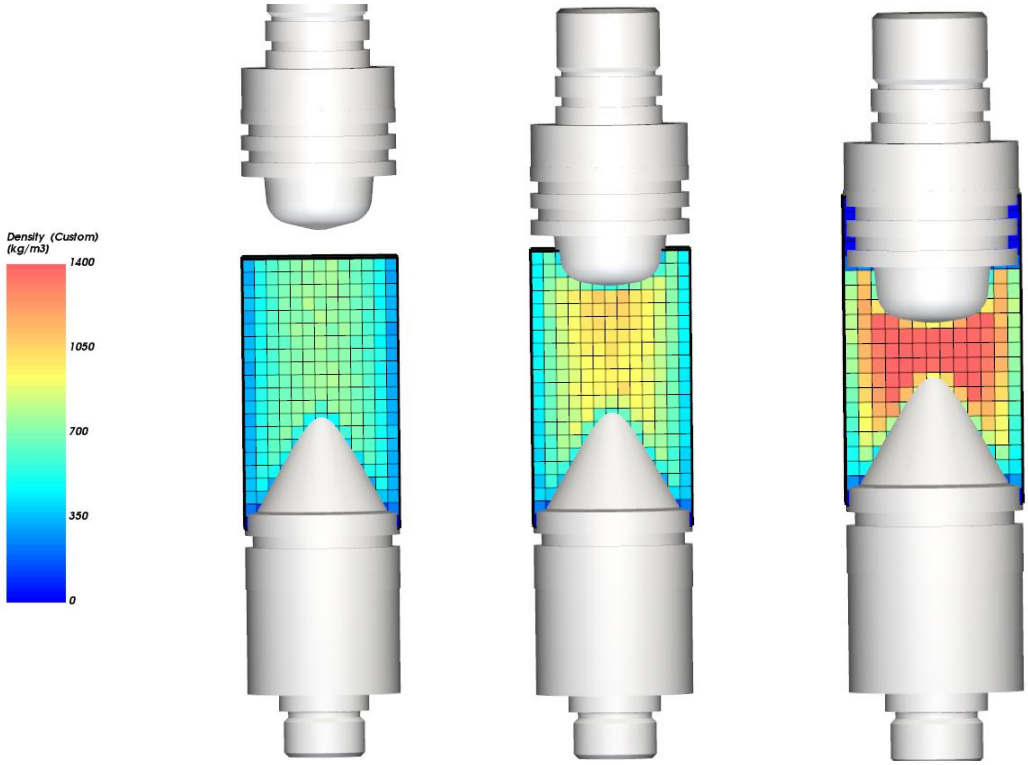

Figure 5.12: Density distribution during the pressing process (grid size is 7.14mm x 6.61 mm).

In the early stage of the process, the density of the central region of the casing experienced a maximum density of 1000 kg/m^3, while the regions close to the wall had lower density.

At the intermediate stage, as the top rammer began to press the material, the material's overall density increased. At the base of top and bottom rammers, the density was less than that of the central region, which achieved a maximum density of 1100 kg/m^3.

As the top rammer descended during the final stage, the overall density increased again. The central region reached a peak density of 1400 kg/m^3. A maximum of 750 kg/m3 occurred in the areas in contact with the wall. The top and bottom corners, by contrast, were almost unaffected by the pressing process.

5.5.3 Discussion of results

Figures 5.10, 5.11, and 5.12 demonstrate that, irrespective of the grid size, uneven density variations in the whole domain were observed in the material during the pressing process. The difference in density values were due to different grid sizes. In small grid size, the particles were larger than the defined volume whereas it was larger than the defined volume in large grid size. This caused to the difference in value among different grid sizes.

Generally, the particles at the beginning of the pressing process displayed relatively low density. As the top rammer pressed into the particles, a clear increase in the density of the material was observed. As the top rammer pressed further into the particles, the density increased further for all grid sizes. Comparable results were observed for all grid sizes, indicating that changing the grid size does not change the density distribution of the material during the pressing process.

5.6 Verification of density distribution

This section compared the density distribution of DEM model output to the real data obtained by Seloane (2018). The output values from the DEM model were compared to the density distribution results obtained from the computed tomography test of an 85-mm diameter casing used by the company. This comparison verified the DEM model's results. The DEM result of small grid size was used to verify the result because it closest result to Seloane (2018).

The simulation result for the density distribution of the material in the casing agreed with the real data provide in Seloane (2018). Results from the simulation are shown in Figures 5.13**,** while the real-life reference data is shown in Figure 5.14. In the simulation, a high-density distribution of about 1400 kg/m^3 occurred in the region between the top and bottom rammer, while the regions close to the base of the bottom rammer (i.e., the top corners of the casing in Figures 5.13) had a medium-density distribution of about 400 kg/m^3. Note also that the distance between the top rammer and bottom rammer for the simulation was the same as the distance between the two in the reference data.

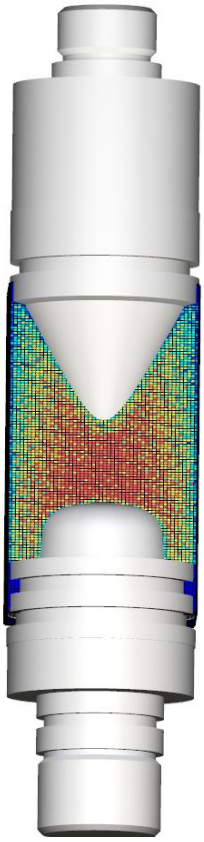

Figure 5.13: Simulation results for density distribution spectrum of the material in casing (small grid size 1.17 mm x 0.67 mm).

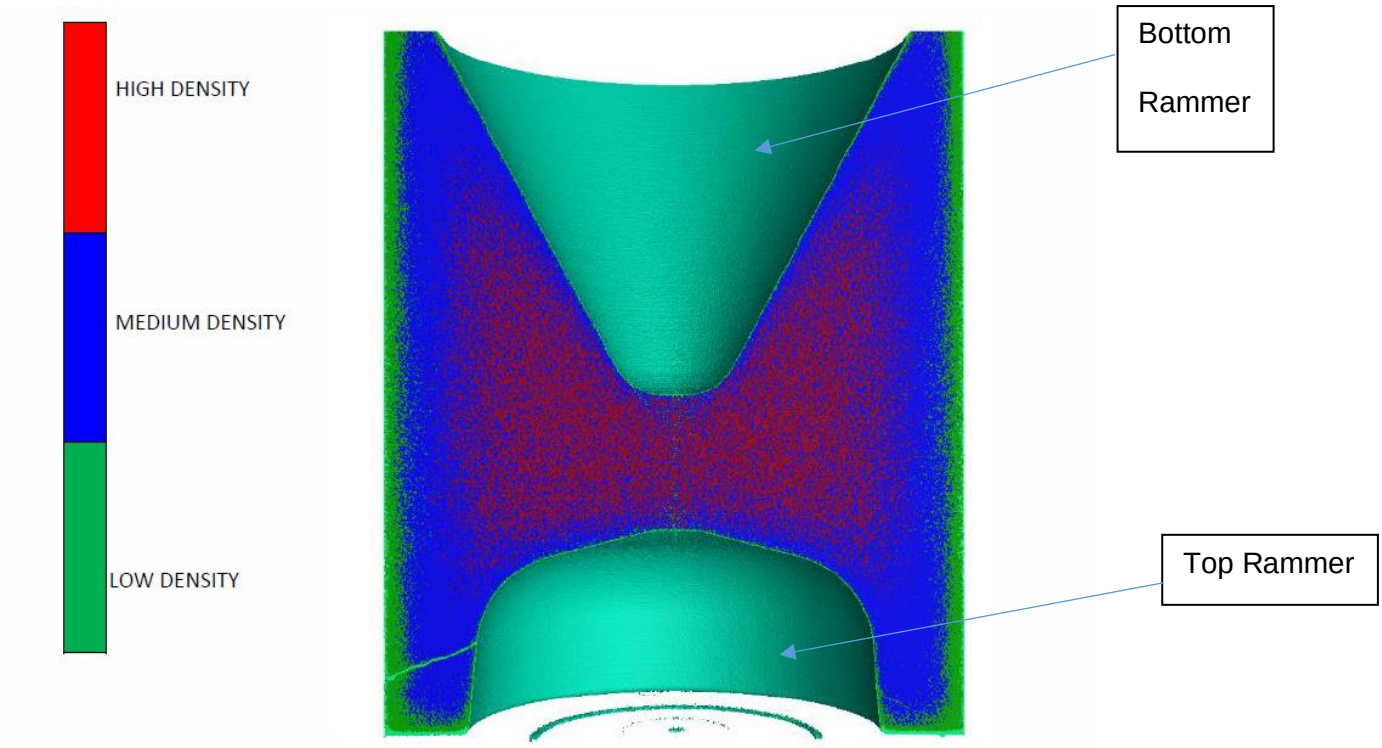

Figure 5.14: Computed tomography result for density distribution in pressed 81 mm casing (Seloane, 2018).

5.7 Summary

In this chapter, DEM was utilised to simulate and study the pressing process. Special care was taken to ensure that the dimensions, characteristics and forces in the simulation mimicked those in the real process used by the company. The pressing simulation was run to obtain results for maximum normal force and density distributions. The density distribution results were in complete agreement with Seloane (2018), suggesting the DEM model was successful. The accuracy was due both to the well-informed material characterisation used for the simulation and the fact that DEM is one of the best tools available for simulating particulate flow. Results obtained for maximum normal force distribution inside the casing via the DEM model showed how the maximum normal force increased with increasing particle size but generally stayed below 400 N. The spectrum plotted for density distribution displayed the expected densely-packed region between the top and bottom rammers, while the regions

around the shell of the casing and around the base of the bottom rammer displayed medium density. Only the regions in contact with the casing displayed low density, suggesting that they are unaffected by the pressing process. This means that the optimum penetration to the target will not be achieved due to uneven density distribution in the 81mm shaped charge.

CHAPTER 6: CONCLUSIONS

6.1 Summary of study

This dissertation examines the use of hydraulic pressing for the manufacture of shaped charges and the applications of numerical modelling techniques incorporating DEM for predicting the density distribution in a shaped charge. The process of hydraulic pressing causes an uneven density distribution of explosive material within a shaped charge. Therefore, this study aims not only to improve the performance of shaped charges, but also to build a model that sheds light on the connection between the pressing process and the performance of shaped charges. Before developing the DEM simulation for the pressing process, it was necessary to determine the particle size and shape distribution for the explosive material. Due to resource and time constraints, particles were classified into three different types of shapes. Bulk density was measured by using relevant equations that consider the volume of the container and the composition of the material filling it. In order to generalise these results, it was necessary to verify the calibration procedure in the same way as for the calibration of samples. The AoR test was used to calibrate static friction coefficients for both the experimental and simulation materials, which proved to be in close agreement with each other.

Subsequently, 3D geometries of the pressing apparatus were imported from AutoCAD program to model the pressing process. Special care was taken to ensure that the dimensions of the apparatus and distance between the liner and the wave shaper after pressing were similar to the real-life setup. Material characterisation was used to provide the material characteristics for the explosive material in the charge. The charge consisted of a casing of 8.5 cm filled with explosive material. The casing was enclosed at both ends by a top and bottom rammer. The top rammer was made to press down into the material in the casing with a force of 58.5 tons. At the moment when the top rammer could not press the material any further, the simulation was stopped and spectrums for the maximum normal force and density distribution were plotted. Due to the special care taken to ensure real life characteristics, the

simulation results obtained for density distribution inside the casing agreed with the real-life reference data available, thus establishing that the simulation was successful. Results for the maximum normal force distribution showed how the force increased with increasing particle size, reaching 1450 N for just a few particles. Most of the material's volume displayed a maximum normal force below 300N. The spectrum for density distribution was also collected from the simulation. This displayed a densely-packed region between the top and bottom rammers. The regions around the rim of the casing and around the base of the bottom rammer mainly displayed medium density, while the area in contact with the casing was mostly unaffected by the pressing process.

6.2 Conclusion and future work

The purpose of this chapter is to provide a concise summary of the research conducted for this study, which seeks to explore the characteristics of shaped charge explosives manufactured via the pressing processes. The research incorporated a numerical modelling technique utilising a DEM technique. The model can accurately predict the density distribution in shaped charges. As a result, the tool can be used to help achieve a more favourable density distribution in shaped charges, which can improve their performance. Additionally, this study confirms that DEM can be used for research involving shaped explosive charges where granular interactions and density distributions determine the quality and performance of the explosive. Further attention should be paid to the task of studying density distribution using different explosive materials and different calibres. Another potential avenue for research is examine the density distribution spectrum when the bottom rammer is made to move upwards, as this might result in a more even density distribution of material inside the casing.

REFERENCES

Asaf, Z., Rubinstein, D., & Shmulevich, I. (2007). Determination of discrete element model parameters required for soil tillage. *Soil and Tillage Research, 92*(1-2), 227-242.

Bourne, B., Cowan, K. G., & Curtis, J. P. (2001). Shaped charge warheads containing low melt energy metal liners. In *Proc. 19th International Symposium on Ballistics, Switzerland*. pp 583-589.

Coetzee, C. J. (2016). Calibration of the discrete element method and the effect of particle shape. *Powder technology, 297*, 50-70.

Coetzee, C. (2017). Review: Calibration of the discrete element method. *Powder Technology*, 310, pp.104-142.

Cundall P. A., & Strack, O. D. L. (1979). A discrete numerical method for granular assemblies, *Geotechnique, 29*(1), 47-65.

Elshenawy, T. A. E. (2012). *Criteria of design improvement of shaped charges used as oil well perforators*. Doctoral dissertation. The University of Manchester, United Kingdom.

Essig, W., Osswald, T.A. & SaBmannshausen, U. (1991). Predicting the density distribution in pressed charges using the finite element method. *Propellants, Explosives, Pyrotechnics, 16*, 73-80.

Garner, S., Strong, J., & Zavaliangos, A. (2018). Study of the die compaction of powders to high relative densities using the discrete element method. *Powder Technology, 330*, 357-370.

Goto, M., Becker, R., Orzechowski, T., Springer, H., Sunwoo, A., & Syn, C. (2007). *Explosively driven facture and fragmentation of metal cylinders and rings*. Livermore, CA: Lawrence Livermore National Lab.

Gröger, T., & Katterfeld, A. (2006). On the numerical calibration of discrete element models for the simulation of bulk solids. Conveying and Handling of Particulate Solids (CHoPS-05). Sorrento, Italy.

James, B. W. (1991). High performance ferrous PM materials for automotive applications. *Metal Powder Report, 46*(9), 26-32.

Kadiri, M. S., Michrafy, A., & Dodds, J. (2005). Pharmaceutical powders compaction: experimental and numerical analysis of the density distribution. *Powder Technology, 15*7(1), 176-182.

Kobylkin, I. F. (2015). Detonation initiation in shielded thin layers of explosives by shaped-charge jets. *Combustion, Explosion, and Shock Waves, 51*(3), 358-365.

Kruggel-Emden, H., Sturm, M., Wirtz, S., & Scherer, V. (2008). Selection of an appropriate time integration scheme for the discrete element method (DEM). *Computers & Chemical Engineering*, *32*(10), 2263-2279. doi: 10.1016/j.compchemeng.2007.11.002.

Head, K. H. (1989). *Soil technicians' handbook*. London: Pentech Press.

Held, M. (2001). Liners for shaped charges. *Journal of Battlefield Technology, 4*(3), 1-7.

Homel, M. A., Guilkey, J., & Brannon, R. M. (2015). Continuum effective-stress approach for high-rate plastic deformation of fluidCha-saturated geomaterials with application to shaped-charge jet penetration. *Acta Mechanica*, *227*(2), 279-310.

Lim, S. (2013). Jet velocity profile of linear shaped charges based on an arced liner collapse. *Journal of Energetic Materials*, *31*(4), 239-250.

Luding, S. (2008). Introduction to discrete element methods: Basic of contact force models and how to perform the micro-macro transition to continuum theory. *European Journal of Environmental and Civil Engineering*, *12*(7-8), 785-826. doi: 10.3166/ejece.12.785-826

Mahdian, A., Ghayour, M., & Liaghat, G. H. (2013). Closed-form model for the analysis of W-type shaped charges. *Journal of Applied Mechanics and Technical Physics*, *54*(5), 713-719.

Nam, H., & Choi, S. J. (2017). Implementation of a semi-implicit time integration scheme in non-hydrostatic Euler equations. *Journal of Applied & Computational Mathematics*, *6*(4). doi: 10.4172/2168-9679.1000369

Noh, G., & Bathe, K. (2013). An explicit time integration scheme for the analysis of wave propagations. *Computers & Structures*, *129*, 178-193. doi: 10.1016/j.compstruc.2013.06.007

Ouye, N., Boeka, D., & Hancock, S. (2007). Material strength effects on shaped charge tip velocities. In *23rd International Symposium on Ballistics.*

Poole, C. J., Ockendon, J. R., & Curtis, J. P. (2002). Gas leakage from fragmentation warheads. In *Proc. 20th International Symposium on Ballistics, Florida*. pp 113-117.

Poole, C. (2005) Penetration of a shaped charge. Doctoral dissertation. Corpus Christi College, University of Oxford.

Rackl, M., & Hanley, K. J. (2017). A methodical calibration procedure for discrete element models. *Powder Technology, 307*, 73-78.

Ransing, R. S., Gethin, D. T., Khoei, A. R., Mosbah, P., & Lewis, R. W. (2000). Powder compaction modelling via the discrete and finite element method. *Materials and Design, 21*(4), 263-269.

Roessler, T., & Katterfeld, A. (2016). Scalability of angle of repose tests for the calibration of DEM parameters. In *12th International Conference on Bulk Materials Storage, Handling and Transportation (ICBMH)*. The Engineers Australia.

Saßmannshausen, U., and Essig, W., & Osswald, T.A. (1989). The density distribution in pressed charges. An analytical approach. *Propellants, Explosives, Pyrotechnics, 14*, 24-27.

Saran, S., Ayısıt, O., & Yavuz, M. S. (2013). Experimental investigations on aluminum shaped charge liners. *Procedia Engineering, 58*(1), 479-486.

Seloane, W. T. (2018). *Investigating density variations within consolidated explosives using experiments to improve their performance and consistency* (Master's thesis). Tshwane University of Technology.

Shi, J., Luo, X., Li, J., & Jiang, J. (2016). Investigation on penetration model of shaped charge jet in water. *Modern Physics Letters, 30*(2), 1-2.

Sinka, I.C., Cunningham, J.C., Zavaliangos, A, 2003. The effect of wall friction in the compaction of pharmaceutical tablets with curved faces: a validation study of the Drucker–Prager Cap model. Powder Technology. 133(1-3): 33–43.

Tadmor, Z. & Gogos, C. (1979). Principles of polymer processing. John Wiley 13 Sons, New York.

Torok, J., Unger, T., Fazekas, S., & Wolf, D. E. (2005). Relationship between particle size and normal force. *Powders and Grains*, 1273-1277. Retrieved from http://www.phy.bme.hu/~torok/files/PandG2005_Torok.pdf

Ugrčić, M., & Ugrčić, D. (2009). FEM techniques in shaped charge simulation. *Scientific Technical Review, 64*(1), 26-34.

Voitenko, Y. I., Goshovskii, S. V., Drachuk, A. G., & Bugaets, V. P. (2013). Mechanical effect of shaped charges with porous liners. *Combustion, Explosion, and Shock Waves*, *49*(1), 109-116.

Walters, W. P., & Zukas, J. A. (1989). *Fundamentals of shaped charges.* John Wiley and Sons.

Yan, G., Yu, H. S., & McDowell, G. (2009). Simulation of granular material behaviour using DEM. *Procedia Earth and Planetary Science, 1*(1), 598-605.

Yan, Z., Wilkinson, S. K., Stitt, E. H., & Marigo, M. (2015). Discrete element modelling (DEM) input parameters: understanding their impact on model predictions using statistical analysis. *Computational Particle Mechanics*, *2*(3), 283–299. doi: 10.1007/s40571-015-0056-5.